university of groningen / faculty of science and engineering

Measuring secondary electrons emitted from ion-surface interactions

Author:
Kristóf NAGY
(s5121981)

Supervisor:
prof. dr. ir. R. A. HOEKSTRA
Daily Supervisor:
L. ASSINK, MSc
Second examiner:
dr. T. A. SCHLATHÖLTER

Bachelor's Thesis
To fulfill the requirements for the degree of
Bachelor of Science in Applied Physics
at the University of Groningen

July 1, 2025

Abstract

The semiconductor industry's continued advancement relies on extreme ultraviolet (EUV) lithography, where energetic laser pulses create tin plasma that emits the 13.5 nm wavelength light. However, this process also produces energetic tin ions that can damage the sensitive mirror optics used to focus the EUV light. This necessitates comprehensive plasma characterization studies, including secondary electron emission from ion-surface interactions. This thesis presents the recommissioning and calibration of an electrostatic analyzer (ESA) for low-energy electron detection in the Sirϕ setup at the Zernike Low-Energy Ion beam Facility (ZERNIKELEIF). This work systematically approaches challenging low-energy electron measurements by studying progressively lower energy systems: Ar^{9+} ions producing autoionization electrons around 210 eV, followed by He^{2+} ions generating electrons near 35 eV through the same process. SIMION simulations characterized the ESA's performance, revealing optimal operating parameters of $F = 6.40$ and $V_{ratio} = -0.910$ at $E_{pass} = 35$ eV, along with an important energy-dependent deviation ranging from +0.04% at 35 eV to -3.53% at 35 keV. Experimental measurements successfully detected characteristic autoionization peaks centered around 207 eV for Ar^{9+} and 36 eV for He^{2+}, showing good agreement with theoretical predictions and literature values. While two distinct autoionization peaks were expected from the latter, only a single peak was observed with energies correctly within the range of the two predicted features. The measurements revealed critical position sensitivity that was addressed through comprehensive setup improvements including installation of a second collimating diaphragm, realignment, elimination of magnetic interference, and enhanced vacuum conditions. These changes enabled successful ion deceleration to much lower energies (450 eV for Ar^{9+} and 10 eV for He^{2+}), increasing autoionization electron yields due to longer interaction times. The calibrated system now provides consistent optimal measurement positions across different ion species and energies, eliminating the need for extensive position optimization when changing experimental parameters. This study provides a foundation for future low-energy electron spectroscopy measurements, particularly for detecting low-energy tin induced secondary electrons relevant to EUV lithography applications.

Contents

1 Introduction

The semiconductor industry has seen unprecedented technological advancement, following the predictions of Moore's Law that computing capacity doubles approximately every 1.5 years. To maintain this pace, modern computer chips require increasingly smaller transistors, pushing the limits of conventional lithography techniques. The Dutch technology company ASML has pioneered the use of Extreme Ultra-Violet (EUV) lithography to meet these demands, utilizing light with a wavelength of 13.5 nm to create patterns with minimum feature sizes that enable the production of state-of-the-art microprocessors.

ASML's EUV lithography systems generate this specific wavelength through laser produced plasma, where CO_2 lasers irradiate Sn droplets to create a plasma that emits photons at the specific wavelength. This light is then focused using mirrors to create intricate patterns on silicon wafers. However, the plasma generation process produces not only the desired EUV photons but also energetic Sn ions with various charge states that can damage the expensive mirror systems. [1]

The detection and characterization of Sn ions requires specialized instrumentation, including retarding field analyzers (RFA), Faraday cups, electrostatic analyzers (ESA), microchannel plates (MCP), and channeltrons. Crucially, all of these detection methods utilize the production of electrons when the ions impact their surfaces to generate measurable electronic signals. This dependence on electron emission makes it essential to accurately characterize the electron spectra from ion-surface interactions.

Sn presents particular challenges in this regard due to its high atomic number, which results in low outer electron binding energies in the tens of eV range. With metal work functions typically around 2-5 eV, this leads to the production of low-energy electrons in the few eV range. These electrons are difficult to detect and measure accurately due to their susceptibility to external influences. To address this challenge a systematic approach is employed here, using different ions with that produce progressively lower characteristic electron energies. First, Ar^{9+} is used, as it was shown to produce an easily detectable single peak at 212 eV [2]. Next, He^{2+} is chosen as it generates lower energy electrons around 35 eV [3]. These steps will enable the accurate measurement of the most challenging low-energy Sn induced electrons in the future. Understanding and characterizing these electron emission processes, particularly for Sn, is essential for accurate measurements of the produced plasma.

The research presented in this thesis was conducted at the Zernike Low Energy Ion-beam Facility (ZERNIKELEIF) at the University of Groningen, where detailed studies of ion interactions are performed. Specifically, this work focuses on the recommissioning and calibration of an ESA in the Surface Physics (Sirϕ) setup for low-energy electron detection.

This thesis presents a comprehensive study of ESA performance and optimization for electron spectroscopy applications. Chapter 2 provides the theoretical background of the relevant physical processes responsible for electron production from ion-surface interactions. Chapter 3 describes the experimental setup, including the ZERNIKELEIF facility, the Sirϕ setup, and the ESA. Chapter 4 presents SIMION simulations of the ESA, investigating optimal operating parameters and characterizing its performance. Chapter 5 details the initial recommissioning phase, presenting the first electron detection tests using Ar^{9+} and He^{2+} ion beams, including peak identification and the discovery of critical position sensitivity. Chapter 6 focuses on systematic improvements to the experimental setup and subsequent calibration measurements, demonstrating enhanced spectral quality and consistent optimal positioning across different ion species and energies. Together, these results aim to establish a robust foundation for future low-energy electron spectroscopy measurements.

2 Theory

When ions interact with a surface, various reaction processes occur that govern charge neutralization dynamics and electron emission. Understanding these processes is crucial for interpreting the low-energy electron spectra observed from ion-surface pairings in this study: Ar^{9+} and He^{2+} ions interacting with metallic surfaces (specifically Ru here).

The reaction processes can be categorized into primary and secondary processes. Primary processes involve direct charge exchange between the projectile and target, with the aim of neutralizing the ion. Secondary processes are de-excitation processes within the projectile afterwards. For this study, autoionization (a secondary process) is the most relevant mechanism, while the primary processes are responsible for creating the initial unstable states. The theoretical framework described below is primarily based on a review of ion-surface interactions [4].

2.1 Primary Reaction Processes

2.1.1 Resonant transitions (RT)

Resonant neutralization (RN) occurs when an electron from below the Fermi energy in the conduction band of the target transfers into an excited level of the incoming ion at the same energy. This process neutralizes the ion without excess energy or direct electron emission. For highly charged ions, resonant transitions occur at large distances above the surface. The energy levels involved in this process are illustrated in Figure 1a. For the Ar^{9+} and He^{2+} ions used in this study, RN is one of the primary mechanisms for creating the excited projectile states which subsequently decay via autoionization.

Quasi-resonant neutralization (QRN) involves electron transfer from a localized core level of a surface atom into a near resonant empty projectile state. Unlike RN, a QRN transition needs the close proximity of the projectile with a surface atom to have sufficient overlap of orbitals. Resonant ionization (RI), the reverse process where an occupied atomic level with a binding energy smaller than the surface work function loses the electron into an empty level of the conduction band above the Fermi level, can also occur but is not relevant for ions used in this study.

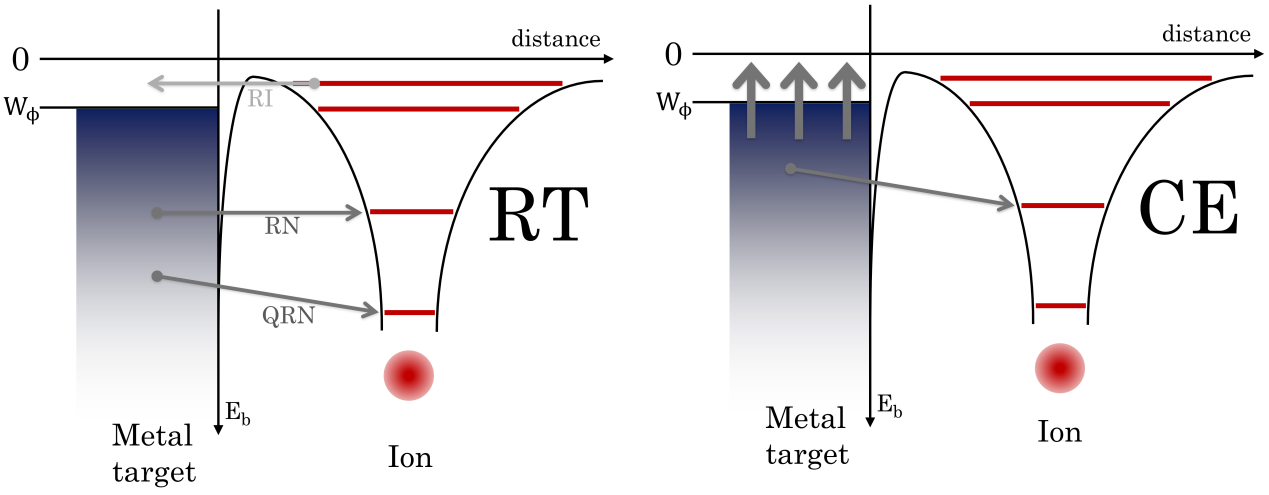

Figure 1: Schematic representations of resonant transitions (a) and collective excitation (b) processes.

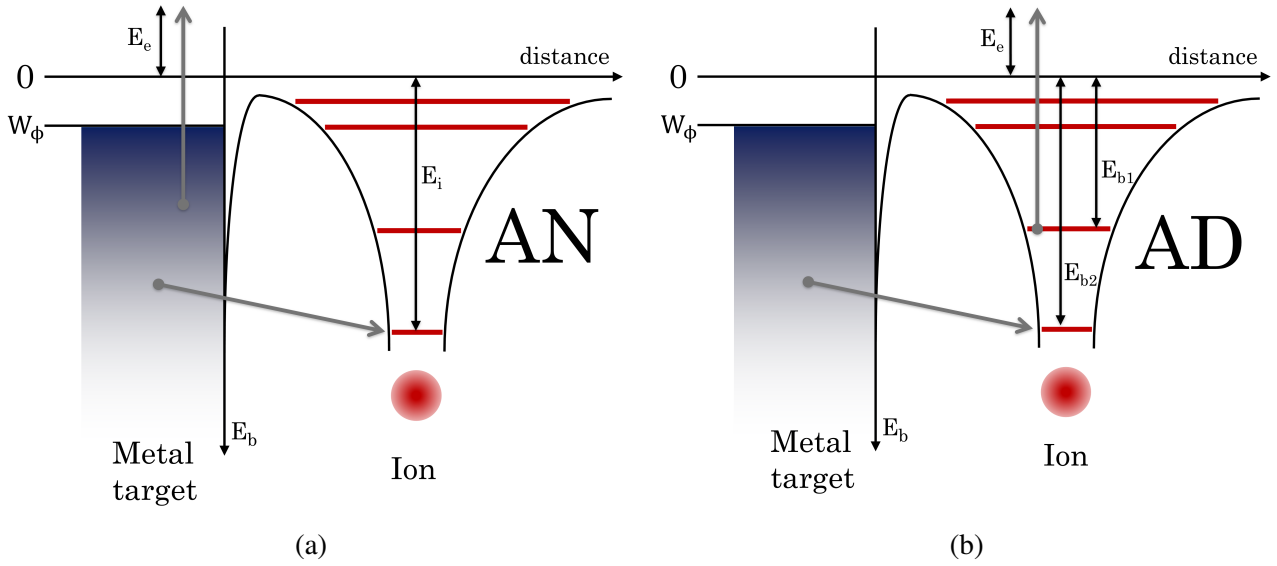

Figure 2: Schematic representations of the Auger neutralization (a) and Auger de-excitation (b) processes.

2.1.2 Collective excitations

In collective excitation (CE), a target electron is captured into a lower projectile state, as illustrated in Figure 1b, but the excess energy creates collective excitations (plasmons) in the target's electronic structure rather than emitting electrons. This process does not directly contribute to the measured electron spectra but could appear as energy loss features. [5]

2.1.3 Auger Neutralization

In Auger neutralization (AN), two electrons from the conduction band are involved. One electron jumps into a deeper lower lying empty level of the ion and another one gains this energy difference, and can be ejected above the vacuum level. This process directly produces electrons, as depicted in Figure 2a.

The kinetic energy E_e of the ejected electron is maximum if both electrons come from the Fermi level:

$$E_e = E_i - 2W_\phi, \tag{1}$$

where E_i is the ionization energy of the captured electron and W_ϕ is the work function. The energy distribution of the emitted electrons is determined by the probability distribution energies at the target's surface: the surface density of states. This results in a broadened energy distribution rather than a sharp peak.

2.1.4 Auger De-excitation

In Auger de-excitation (AD) is a higher level electron from the projectile is emitted when an electron from the target's conduction band jumps into a deeper vacant level in the ion. The role of the two electrons is swapped compared to AN, as shown in Figure 2b.

The maximum energy of the ejected electron is:

$$E_e = (E_{b1} - E_{b2}) - W_\phi, \tag{2}$$

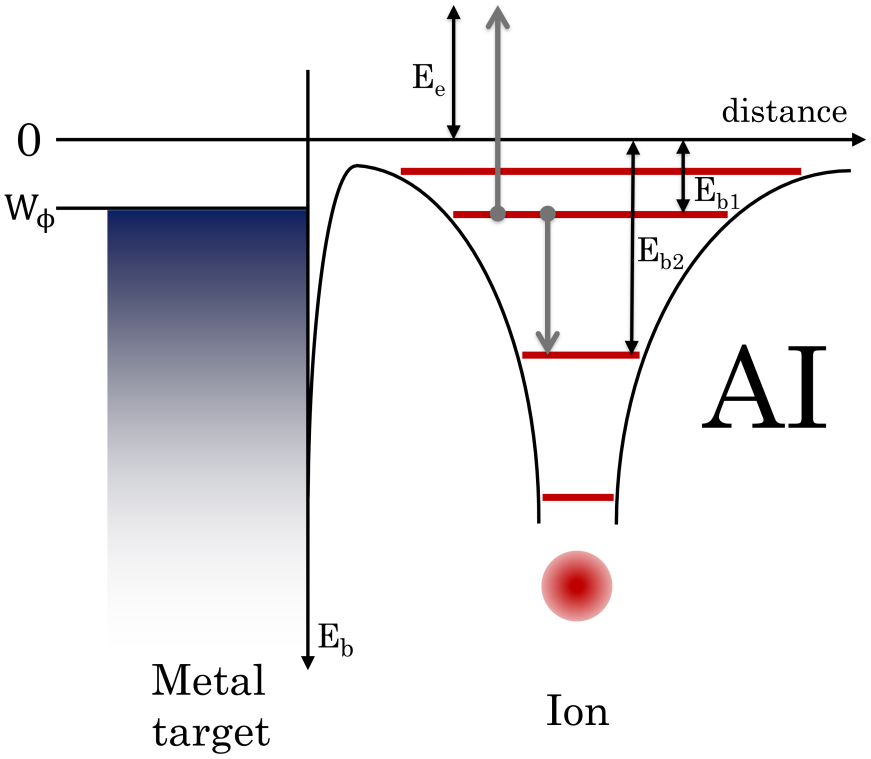

Figure 3: Schematic representation of autoionization (AI).

where $(E_{b1} - E_{b2})$ is the difference in excitation energy of the of the two involved energy levels of the projectile. Like AN, this process contributes to broader spectral features rather than sharp peaks.

2.2 Secondary Reaction Processes

2.2.1 Autoionization

In autoionization (AI) two electrons of the now neutralized, but unstable projectile are involved. One excited electron jumps into a lower lying vacant level while the other excited electron is ejected. Since both electrons in autoionization originate from well-defined energy levels of the projectile atom, they produce sharp peaks with relatively narrow energy distributions in the spectrum, making this process ideal for characterizing the ESA. The energy levels involved in this process is illustrated in Figure 3.

The kinetic energy of the emitted electrons is given by the difference in binding energies:

$$E_e = E_{b1} - E_{b2}, \tag{3}$$

where E_{b1}, and E_{b2} represent the binding energies of the initial and final states, respectively.

2.2.2 Radiative decay

Radiative decay (RD) occurs when an electron in an ion transitions to a lower energy state, and the excess energy is carried away by an emitted photon. This process contributes only minimally to the studied de-excitation mechanisms and produces no electrons.

3 Experimental Setup

All experiments were conducted at the Zernike Low-Energy Ion beam Facility (ZERNIKELEIF) at the University of Groningen, within the Quantum Interactions and Structural Dynamics (QISD) research group. This facility provides worldwide unique capabilities for low-energy ion interaction studies, particularly for tin. The experimental approach relies on systematic measurement of electron emission spectra from ion-surface interactions. The relevant components of the setup are: the ion source and beamline system for ion generation and transport, the Surface Physics (Sirϕ) experimental setup with its μ-metal vacuum chamber, and the electrostatic analyzer (ESA) for electron energy spectra acquisition. Together, these components enable precise control over ion beam parameters and detailed analysis of surface interaction processes.

3.1 ZERNIKELEIF: Ion Source and Beamline

Ion beams are generated using a 14 GHz Electron Cyclotron Resonance Ion Source (ECRIS). The source uses a permanent magnet system to create a strong magnetic field that confines the plasma. The kinetic energy (E_k) of ions extracted from the source is determined by the source potential (V_{source}) and the ion charge state (q): $E_k = q \cdot V_{\text{source}}$.

After extraction, the ion beam passes through a 110° analyzing magnet that selects ions based on their mass-to-charge ratio (A/q). This ensures that only ions of the desired species enter the beamline. The beam then travels through three quadrupole triplet magnets (QT) that focus it to reduce divergence. Correction magnets (CM) along the beamline minimize shifts in the beam's trajectory. Finally, a 45° bending magnet directs the beam into the Sirϕ setup. See Figure 4 for a schematic overview of this path.

3.2 Sirϕ

The Surface Physics (Sirϕ) experimental setup serves as the central interaction chamber where ion-surface collisions occur and secondary particles are analyzed. Its core is a 300 mm diameter μ-metal vacuum chamber that prevents external magnetic fields from affecting measurements and is

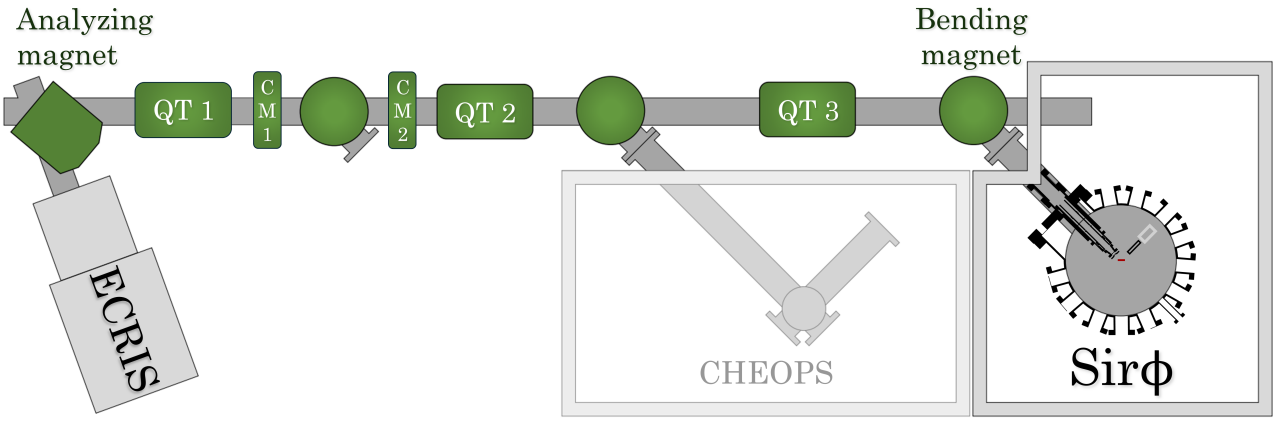

Figure 4: The ZERNIKELEIF facility features an ECR Ion Source, followed by a 110° analyzing magnet for A/q selection. The beam then passes through three quadrupole triplet magnets (QT) for focusing, correction magnets (CM) for trajectory optimization, and finally a 45° bending magnet that directs the ion beam into the Sirϕ experimental setup.

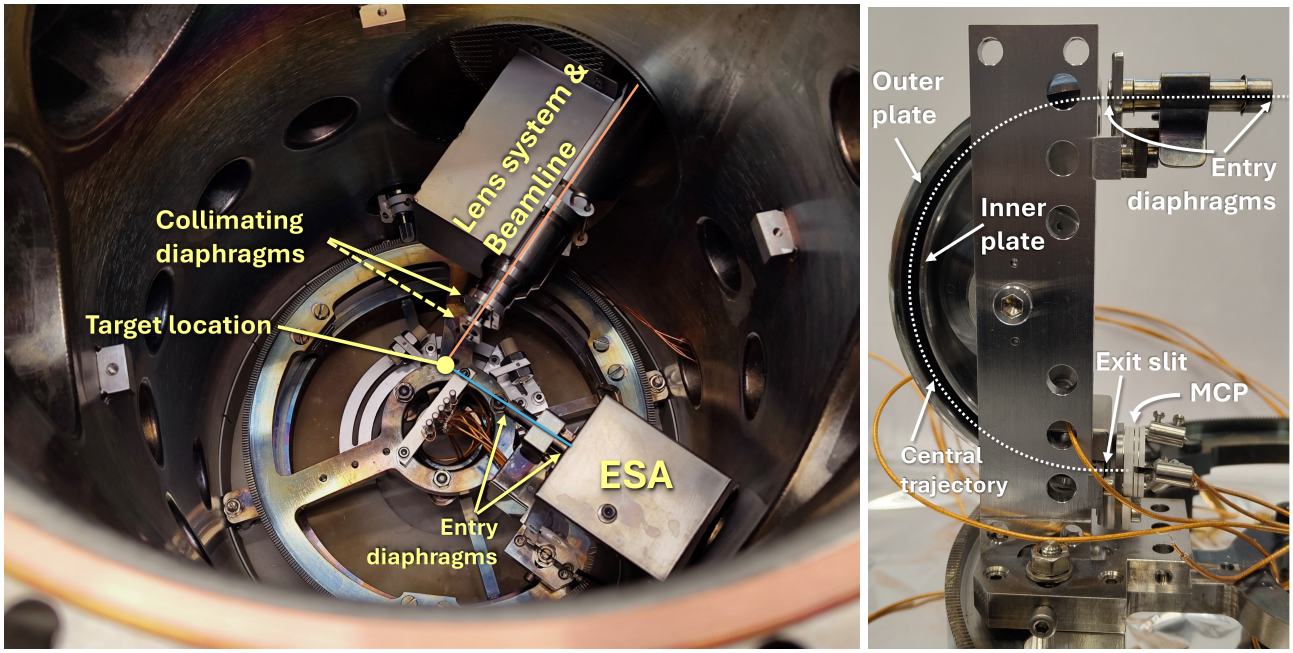

(a) (b)

Figure 5: Photographs of the Sirϕ experimental setup components. The Sirϕ vacuum chamber (a) shows the ion beam path (orange) to the target and the ESA's electron detection view (blue). The second collimating diaphragm is also already installed (dashed arrow). The μ-metal chamber provides magnetic shielding and is maintained at ultra-high vacuum. A side view (b) of the ESA with its μ-metal shielding removed reveals entry diaphragms, concentric hemispherical plates, and the MCP detector.

maintained at an ultra-high vacuum of $\sim 5^{-10}$ mbar using an ion pump. The setup incorporates a deceleration system for precise ion energy control, a five-axis target manipulator for positioning, and multiple detection capabilities including time-of-flight (TOF), retarding field analyzer (RFA), and electrostatic analyzer (ESA) measurements. Figure 5a shows an internal view of the Sirϕ setup.

3.2.1 Deceleration System

Ion deceleration is achieved by floating the entire Sirϕ setup at high voltage, including all electronic systems. This creates a potential difference that slows down the ions as they approach the target. The final kinetic energy of the ions at the target is given by: $E_{\text{kin}} = q \cdot V_{\text{bias}}$, where V_{bias} is the difference between V_{source} and the setup's new ground potential. V_{bias} is controlled directly using a Fluke high voltage power supply, while the setup is isolated from the beamline using a ceramic insulator. This deceleration system is essential as it allows ion energies to be reduced from the initial keV range down to eV levels, which increases the interaction time spent in front of the surface.

Before entering the main chamber, the ion beam passes through a deceleration lens system consisting of four electrostatic lenses (labeled B-E). These lenses guide the ions through the changing potential field, and focus the beam during both regular and decelerated measurements. The beam finally enters the chamber through a 2 mm collimation diaphragm. An additional 1.5 mm diameter diaphragm can be added after the first one; this configuration was used in Section 6, and is also depicted in Figure 5a.

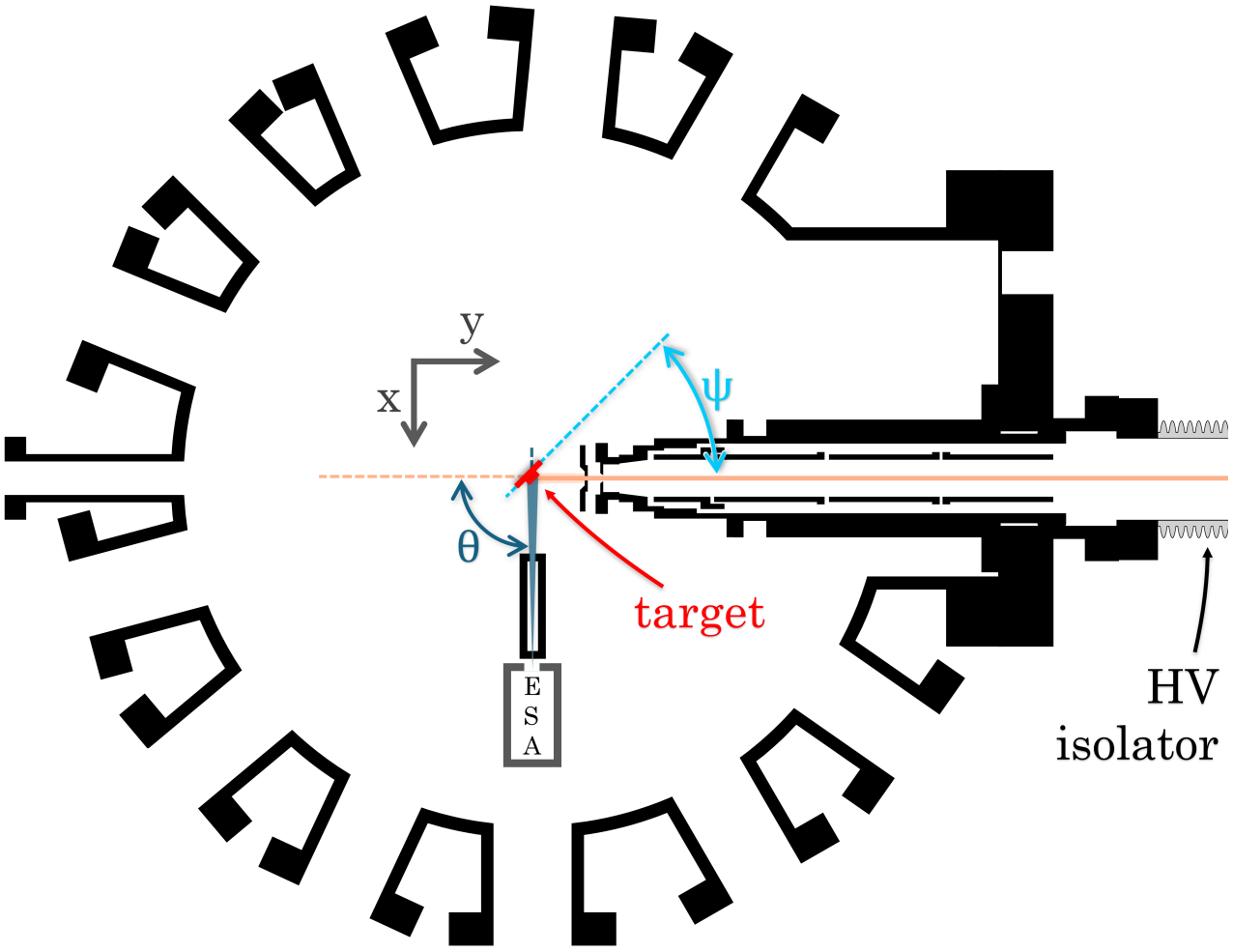

Figure 6: Overview of the Sirϕ experimental setup's geometry, showing the coordinate system and angular definitions used. The target manipulator provides translational motion in the *x*-*y* plane and rotational control of the angle between incoming beam and target surface (ψ). The ESA can be positioned around the chamber on a track system, changing the detection angle θ. Not shown are *z* and ϕ as they both remained fixed for this study. The high voltage isolator is also indicated, it is essential when biasing the setup for decelerating.

3.2.2 Target Manipulator and Geometry

The target is mounted on a five-axis manipulator system that provides precise control over position and orientation. It allows translational motion of 25 mm in the *x*-*y* plane (in the beam plane) and 400 mm in the *z*-direction (perpendicular to the beam). Two rotational motions are available: the target angle ψ (angle between the incoming beam direction and the target surface) and the azimuthal angle ϕ (a rotational axis along the surface normal). Additionally, the ESA itself can be moved around the center of the chamber on a track system, giving the detection angle θ between the incoming beam direction and the detector position. Figure 6 shows the layout of relevant angles and axes used in this study.

Several constraints are applied during experiments. To eliminate Doppler shift effects on the measured electron energies, the ESA has to be positioned at $\pm 90^\circ$ relative to the beam [2]. $\theta = 90^\circ$ was chosen as the track system can cause changes in the vertical alignment for $\theta < 0$. The *z*-coordinate

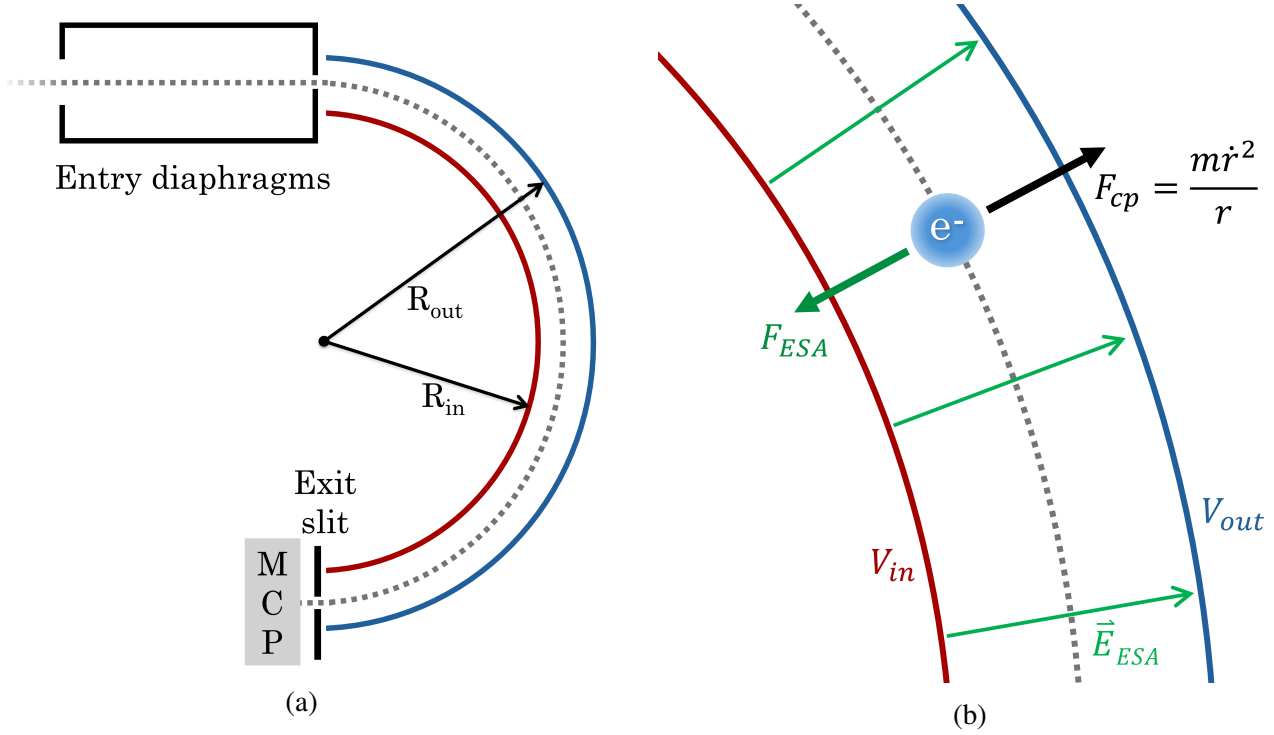

Figure 7: Operating principles of the electrostatic analyzer (ESA). Cross-sectional schematic (a) showing the concentric hemispherical plates with $R_{in} = 48$ mm and $R_{out} = 52$ mm, where voltages V_{in} and V_{out} create an electric field for energy-selective charged particle detection. A force diagram (b) illustrates the balance between centripetal forces F_{cp} and the electrostatic force F_{ESA} created by this electric field.

(target height) and azimuthal angle (ϕ) also remained fixed throughout all measurements to simplify geometrical analysis and maintain consistent alignment. This left the x and y positions to be adjusted in order to find the optimal position with the best signal quality.

3.2.3 Electrostatic analyzer (ESA)

The electrostatic analyzer is a 180° semi-hemispherical detector that measures the energy distributions of charged particles from the target surface. The ESA is depicted in Figure 5b.

The ESA consists of two concentric hemispherical plates with the inner having radius $R_{in} = 48$ mm and outer $R_{out} = 52$ mm, as shown in Figure 7a. When voltages V_{in} and V_{out} are applied to the inner and outer plates respectively, an electric field is created between them. A charged particle can only pass through the ESA when the perceived outward centripetal force equals the inward electrostatic force ($F_{cp} = F_{ESA}$). This situation is depicted in Figure 7b.

For a particle with mass m and charge q traveling along radius r, this force balance gives:

$$\frac{m\dot{r}^2}{r} = \frac{q(V_{out} - V_{in})R_{in}R_{out}}{(R_{out} - R_{in})r^2}.$$

For a particle with kinetic energy $E_k = m\dot{r}^2/2$ to be detected, it must travel through the central trajectory $r = (R_{in} + R_{out})/2$ and pass through the exit slit before reaching the microchannel plate (MCP) detector. This leads to the condition:

$$E_k = q(V_{out} - V_{in}) \cdot F, \tag{4}$$

where F is the proportionality factor:

$$F = \frac{1}{R_{out}/R_{in} - R_{in}/R_{out}}. \tag{5}$$

Plugging in the radii the, theoretical values $F = 6.24$ and $V_{ratio} = V_{out}/V_{in} = -0.923$ can be obtained. However, for this semi-hemispherical geometry, the empirically determined values $F = 6.42$ and $V_{ratio} = -0.935$ are used [3, 6]. The ESA measures the pass kinetic energy $E_{\text{pass}} = E_k/|q|$, meaning particles with different charge states but the same kinetic energy per charge will be detected at the same voltage settings. This is not a concern when measuring electrons ($q = -1$).

The energy resolution of the ESA is characterized by a constant ratio $\Delta E/E_{\text{pass}}$, with the theoretical value for this resolution being 0.5% [3]. Due to this constant relative resolution, it has to be taken into account that the absolute energy bin width increases with energy.

To ensure accurate analysis, several corrections are applied to account for experimental factors. Beam current fluctuations are corrected for by normalizing to the measured target current, while the energy resolution is accounted for by dividing by ΔE. These normalizations result in corrected yield spectra with units of counts per nanoCoulomb per eV (/nC/eV).

4 Simulations of the ESA

Understanding the performance characteristics and optimal operating conditions of the electrostatic analyzer (ESA) requires modeling of charged particle behavior through the analyzer's electric field configurations. This is achieved using SIMION, a specialized software package designed for simulating electromagnetic fields and charged particle dynamics in complex geometries.

SIMION operates by discretizing space into a grid of equally spaced points and solving Laplace's equation at each grid point to determine the electric potential distribution. Users can define electrode geometries by designating clusters of grid points, with each electrode capable of being biased independently. The software then calculates particle trajectories by computing the Coulomb and Lorentz forces acting on charged particles at each time step. The simulations shown here were performed using a 3D model of the ESA designed by Mart Salverda.

The performance of the ESA is quantified through two primary metrics derived from the energy distribution of electrons that successfully pass through the analyzer. The accuracy of the pass energy is evaluated relative to E_{pass}. This is done by calculating the E_{pass} deviation (%): $100 \times (1 - E_{observed}/E_{pass})$, where $E_{observed}$ is the mean of the Gaussian fitted to the transmitted energy distribution. This metric represents how the energy measured by the ESA deviate from a particle's actual kinetic energy. Additionally, the energy resolution is characterized by measuring the full width at half maximum (FWHM) of the same Gaussian. While all simulations presented here were performed using electrons, one can expect ions to exhibit similar behavior given that the electrostatic principles governing their trajectories are the same.

In this chapter, comprehensive SIMION simulations of the ESA are presented to characterize its performance. The simulations address three key objectives: first, determining the optimal proportionality factor F and voltage ratio V_{ratio} for this simulated geometry; second, characterizing the energy dependence of its performance; and third, investigating the effect of entrance position on the observed energy distribution. These computational studies provide crucial insights for maximizing the analyzer's performance before experimental implementation and help establish the theoretical framework for interpreting measured electron spectra.

4.1 Finding an optimal F and V_{ratio}

To determine the optimal operating parameters for this ESA, systematic simulations were conducted using 10^5 electrons per simulation run with a uniform energy distribution between 30 and 40 eV. The electrons were initialized 34 mm in front of the first entry diaphragm with a cone-shaped uniform direction distribution of 0.16° (sufficient to cover the second diaphragm). The voltages V_{in} and V_{out} were calculated for $E_{pass} = 35$ eV using Equations (4) and (5), while the front of the MCP was maintained at 100 V to mirror experimental conditions.

A comprehensive parameter sweep was performed by varying F from 5.50 to 7.00 in steps of 0.15, while simultaneously adjusting $V_{ratio} = V_{out}/V_{in}$ from -0.825 to -1.250 in steps of -0.0425. This gave 121 unique combinations to be simulated, each with corresponding calculated values of V_{in} and V_{out} set.

The initial analysis of the parameter sweep shown in Figure 8a revealed that $F = 6.40$ consistently produced the smallest deviation from E_{pass} across all tested voltage ratios. As shown in Figure 8b, FWHM showed no correlation with either F or V_{ratio} parameters, if enough particles from the initial 30-40 eV distribution passed through the ESA.

To refine the optimization, the E_{pass} deviation was examined as a function of V_{ratio} while maintaining $F = 6.40$ constant, resulting in Figure 9a. It shows a clear linear relationship between V_{ratio} and

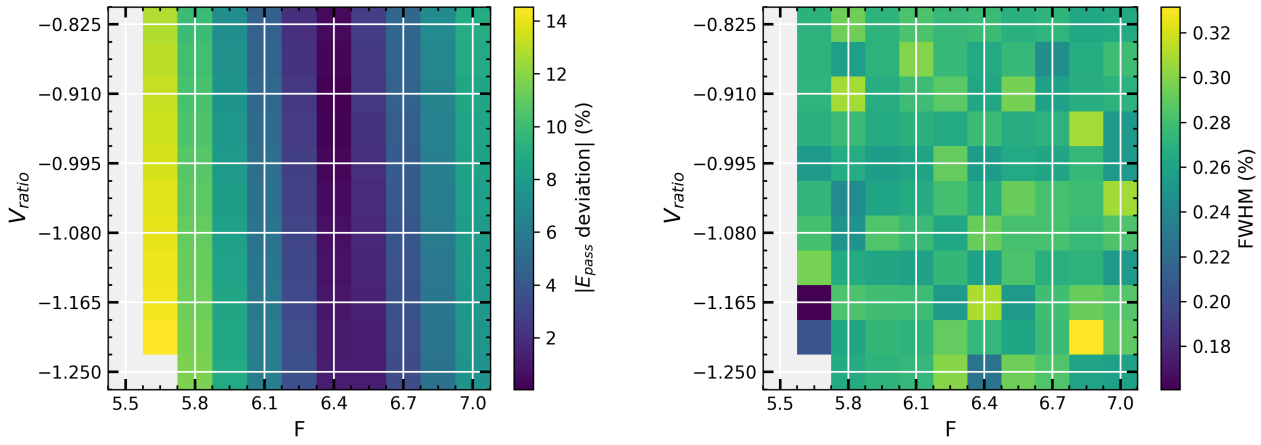

(a) (b)

Figure 8: Parameter sweep results for ESA optimization at $E_{pass} = 35$ eV. The absolute ratio of deviation from the pass energy as a function of proportionality factor F and voltage ratio V_{ratio} (a), with the column $F = 6.40$ showing the closest values. FWHM as a function of the same parameters (b) demonstrates the lack of systematic correlation between energy resolution and the two parameters.

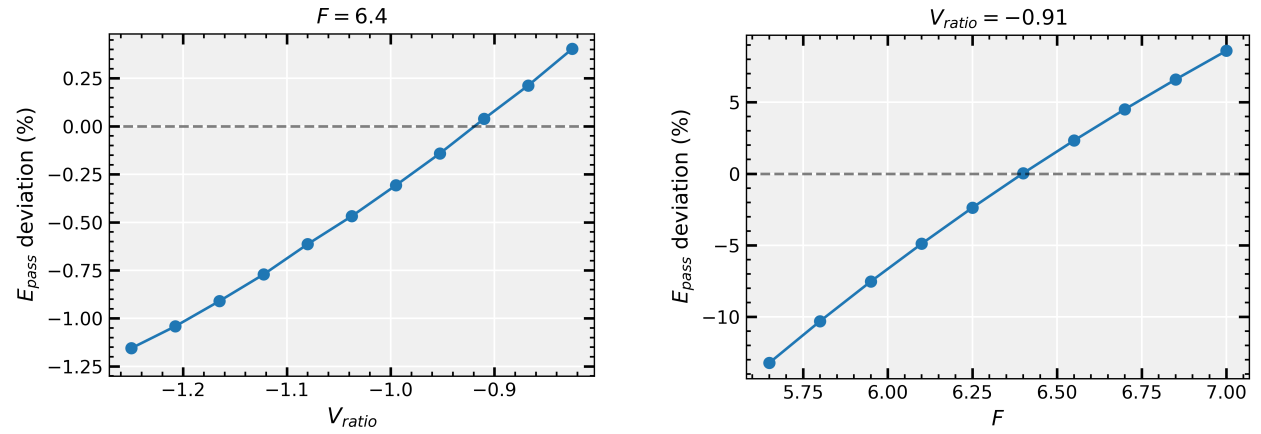

(a) (b)

Figure 9: Linear optimization relationships for ESA parameters. E_{pass} deviation compared to $E_{pass} = 35$ eV as a function of voltage ratio V_{ratio} with F fixed at 6.40 (a), reaching minimum deviation at $V_{ratio} = -0.910$. And the deviation as a function of proportionality factor F with V_{ratio} fixed at -0.910 (b), confirming the optimal value of $F = 6.40$.

the energy deviation, with $V_{ratio} = -0.910$ identified as the optimal value within the tested range.

Conversely, when V_{ratio} was held constant at -0.910 and F was varied, a similar linear relationship emerged, as seen in Figure 9b. This has also further confirmed $F = 6.40$ as the optimal F value.

The optimized parameter combination ($F = 6.40$, $V_{ratio} = -0.910$) achieved a high accuracy with only 0.04% deviation from E_{pass} and an FWHM of 0.26%. Note, that this small deviation could be further reduced with simulations using finer parameter steps near these optimal values. The resolution represents approximately half of the expected 0.5% [3], attributed to the idealized simulation condition where all particles originate from a single location rather than a more realistic distribution of

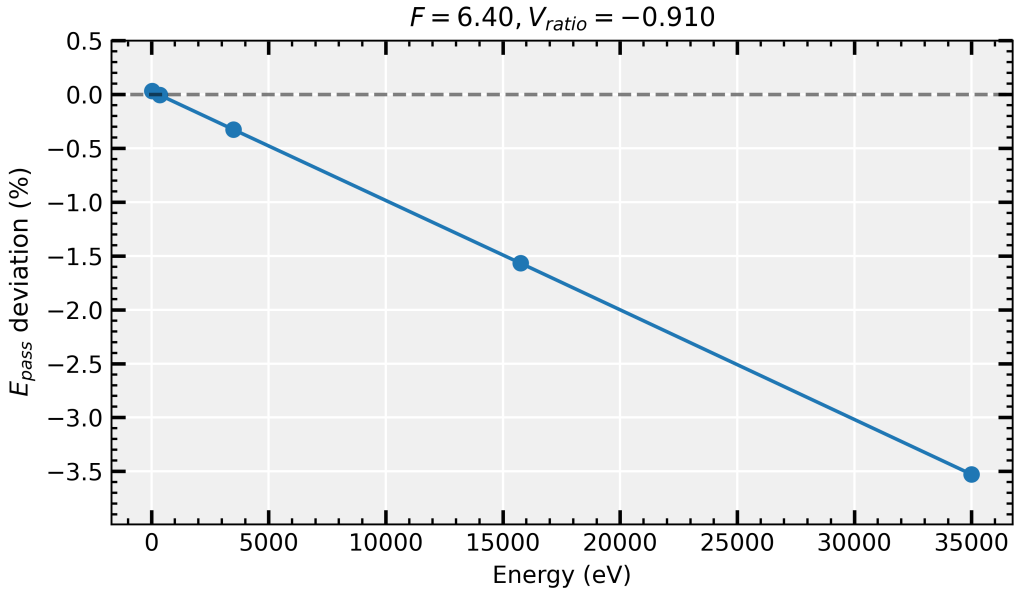

Figure 10: Energy dependence of ESA performance showing deviation from the pass energy as a function of the energy regime given by E_{pass}. The linear trend reveals a steady shift from positive to negative deviations with increasing energy, starting from $+0.04\%$ at 35 eV to -3.53% at 35 keV.

starting positions. The effect of spatial distribution on performance is investigated further in Section 4.2.

To verify the energy-independence of these optimization results, the parameter relationships were tested at a higher energy regime. Some simulation of the original 121 were repeated with an energy range of 3000-4000 eV and $E_{pass} = 3500$ eV while maintaining all other parameters constant. The deviations in pass energy exhibited identical behavior across both energy regimes, as demonstrated by the strong correlation seen in Figure A.2 of the Appendix. This confirms that the electrostatic principles governing the optimization are energy-independent, as theoretically expected. The FWHM showed no correlation between the 35 eV and 3500 eV results (see Figure A.3 in the Appendix), consistent with the lack of F or V_{ratio} dependence observed at 35 eV.

4.2 Energy dependence

To evaluate the ESA's performance across its operational energy range, simulations were conducted using the optimized parameters ($F = 6.40$ and $V_{ratio} = -0.910$) with 10^5 electrons from the same single point and identical conical distribution, as in the section above. Uniform energy distributions were applied between 3×10^n and 4×10^n eV with corresponding $E_{pass} = 3.5 \times 10^n$ eV set, where n was varied from 1 to 4, with an additional step between $n = 3$ and 4 added.

A significant energy-dependence of the E_{pass} deviation ratio was observed. As shown in Figure 10, the deviation in pass energy exhibits a steady trend across the energy range. At the lowest energy ($E_{pass} = 35$ eV), the deviation was minimal at +0.04%, as it was optimized for this energy in the previous section. However, the deviation increased linearly to -3.53% at $E_{pass} = 35$ keV. This meant that when the ESA was configured for a pass energy of 35 keV, the observed mean energy was actually 36.235 keV.

The energy resolution, characterized by the FWHM, showed no obvious trend with increasing energy, as illustrated in Figure A.4 in the Appendix. However, given that all FWHM values remained within the broad range observed during parameter optimization (comparable to the variations seen in Figure 8b and Figure A.3 which can be found in the Appendix), no definitive conclusions regarding energy-dependent resolution degradation can be drawn.

To investigate potential effects of the simulation approach used, the influence of the MCP front voltage was examined, as this parameter had been held constant at 100 V across all energy ranges. However, as demonstrated in Figure A.5 of the Appendix, no correlation was found between the front voltage and either of the metrics, ruling out this as a contributing factor to the observed energy dependence.

The -3.53% shift at high energies is unexpected, as electrostatic relationships are expected to scale proportionally with particle energy. This energy-dependent deviation may partially explain the discrepancy between the computationally optimized parameters ($F = 6.40$, $V_{ratio} = -0.910$) and those determined through experimental calibration of the actual setup ($F = 6.42$, $V_{ratio} = -0.935$) [3, 6]. As the experimental parameters may have been optimized for a different and higher energy range.

This energy dependence has important practical implications for spectroscopy measurements performed using this experimental setup. When analyzing particles with energies significantly different from the calibration energy, the ESA will have a consistent error in observed energies. For calibration energies much lower than the energies to be measured, shifts toward lower values occur. While calibration at significantly higher energies compared to the measured ones would result in shifts toward higher energies. To mitigate this effect, it would be beneficial to calibrate the ESA across multiple energy points and implement energy-dependent corrections to the F and V_{ratio} parameters during data acquisition.

4.3 Position dependence of the energy distribution

To assess the ESA performance under more realistic conditions, simulations were conducted modeling the spatial distribution of particles entering the analyzer. In the actual experimental setup, particles reaching the ESA originate from within a $d = 3.82$ mm diameter circle on the target when positioned at $\psi = 45^\circ$ and $\theta = 90^\circ$ [6].

To simulate this scenario, 10^7 electrons (the maximum number supported by SIMION) were initialized within a uniform spherical distribution with $d = 4$ mm diameter. This sphere was centered at the same location used in previous sections, 34 mm in front of the entry diaphragm, to accurately represent the target's position in the Sirϕ setup. The directional cone distribution was expanded to 2.75° to ensure particles from all positions within the sphere could reach the second entry diaphragm. The energy distribution was narrowed to 33-36 eV to improve transmitted particle statistics. The pass energy was maintained at $E_{pass} = 35$ eV, using the previously optimized parameters ($F = 6.40$, $V_{ratio} = -0.910$).

The spatial distribution of particle origins significantly affected the transmitted energy spectrum. As shown in Figure 11, the FWHM increased to 0.40%, approaching the theoretical expectation of 0.5% [3]. However, the spectrum also exhibited an asymmetric broadening, with a distinct lower-energy region extending between 34.1 and 34.8 eV. This asymmetric behavior warranted further investigation, as it deviated from the symmetric Gaussian profile one could expect.

To understand the origin of this asymmetric broadening, particle trajectories were analyzed for three representative energies: 34.34 eV (low-energy region), 34.65 eV (intermediate), and 34.975 eV (main peak), as indicated in Figure 11. The trajectory analysis revealed that particles contributing to the low-energy section consistently travel along paths very close to the inner cylindrical plate, as

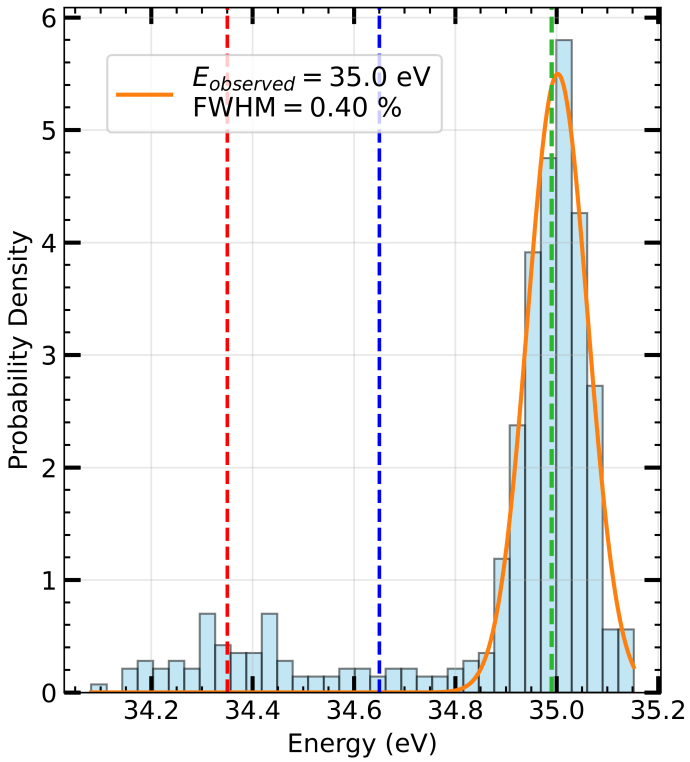

Figure 11: Energy distribution of electrons transmitted through the ESA when initialized from a 4 mm diameter spherical distribution. The spectrum shows the expected main peak centered around 35 eV with FWHM of 0.40%, but also exhibits an asymmetric low-energy region. The three color marked energies correspond to the particle trajectories analyzed in the 3D visualization of Figure 12.

shown in Figure 12a. The front view in Figure 12b revealed that the lower-energy particles exhibit a slight preference for the left side. This lateral asymmetry can be attributed to the ESA's design: the cylindrical plates are open on the right side, creating a slightly non-uniformity in the electric field.

The correlation between particle trajectories and their initial positions was further investigated by examining the spatial distribution of the starting point of successfully transmitted particles. Figure 13 shows the starting positions of all transmitted particles as viewed from the entrance of the ESA, colored by their energies. The analysis reveals that particles making up the low-energy region predominantly originate from the upper half of the initial spherical distribution, with a slight bias toward the left side.

Overall, the low-energy region, while clearly present, accounts for only a small fraction of the total transmitted particle count compared to the main peak. Given this limited magnitude, the practical impact on spectroscopic measurements is likely minimal, and implementing aperture restrictions to mitigate this effect would not justify the resulting reduction in field of view. The existing constraints already necessitate precise alignment and positional tuning, challenges that will be explored in the following sections.

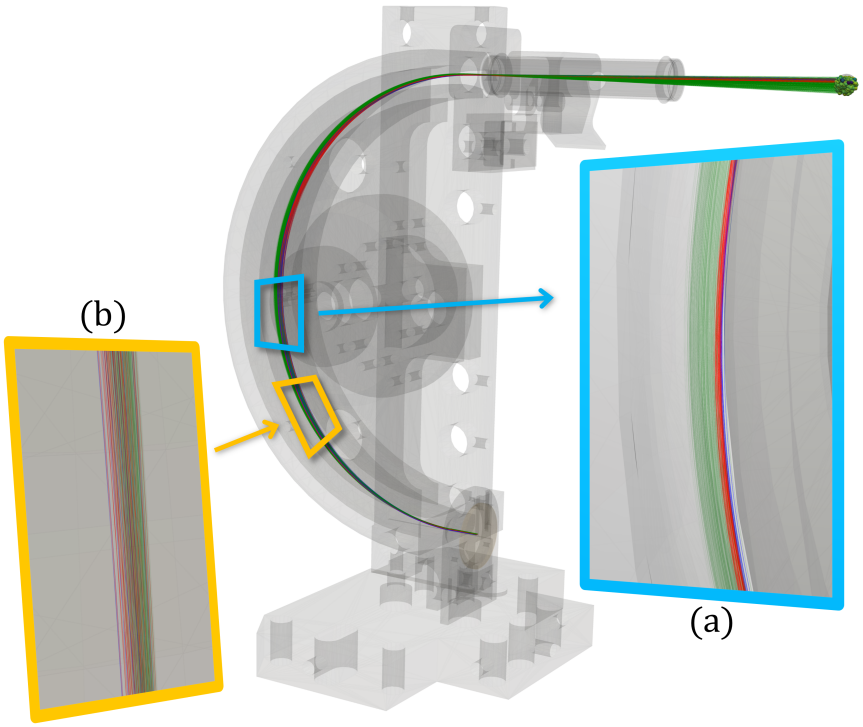

Figure 12: Three-dimensional particle trajectories for electrons with energies of 34.34 eV (red), 34.65 eV (green), and 34.975 eV (dark blue). The side view (a) demonstrates that low-energy particles follow trajectories closer to the inner cylindrical plate, while the front view (b) shows a slight preference for the left side of the hemispherical channel for the low-energy particles.

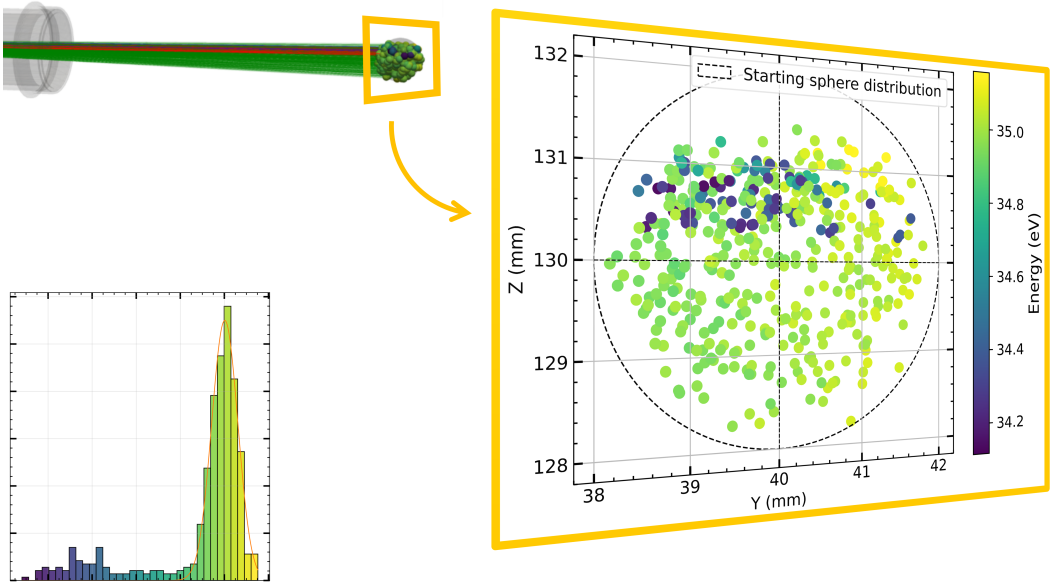

Figure 13: Spatial distribution of initial particle positions for successfully transmitted electrons (right), viewed from front of the ESA entrance. The coloring corresponds to the transmitted particle energies, showing that particles originating from the upper portion of the $d = 4$ mm sphere are responsible for the low-energy region observed. Figure 11 is repeated (bottom-left) with matching coloring.

5 Recommissioning the ESA for electrons

This chapter presents the first electron energy spectra obtained with the electrostatic analyzer (ESA) following its recommissioning for electron measurements. Expected autoionization peaks for Ar^{9+} and He^{2+} ions are first established from theoretical calculations and previous experimental work, then compared with the initial experimental results. The main challenge encountered was the strong dependence of spectral quality on target positioning, which varied with both beam energy and deceleration lens settings and required extensive optimization.

5.1 Expected peaks

Ar^{9+}

The complex electron structure of argon makes conclusive theoretical predictions difficult, however, extensive experimental data is available for comparison. Electron impact excitation of Ar gas produces emission peaks across a wide energy range, with a region of particularly high intensity between 201.09-207.23 eV and most prominent peak occurring at 205.21 eV [7]. Previous surface-ion experiments using a similar configuration of the Sirϕ setup yielded a broader peak centered at 212 eV in 1989 [2].

He^{2+}

For doubly ionized helium, theoretical calculations are more readily available due to the limited number of states. Table 1 summarizes the relevant doubly excited helium states along with their corresponding calculated electron kinetic energies (E_e), determined using Equation (3). Based on the autoionization rates (Γ_{AI}) and statistical weights (g_i) of each state, two distinct peak regions are anticipated: one around ~ 33.5 eV and another around ~ 35.4 eV.

For successful observation of the emitted electrons, the autoionization process must occur before the excited He^{**} reaches the surface. Based on the state's lifetimes, this requires the use of low ion velocities to increase the interaction time spent in front of the surface.

State	E_{b1} (eV)	E_{b2} (eV)	E_e **(eV)**	Γ_{AI} (10^{14} Hz)	g_i	Lifetime (fs)
$(2s^2)^1$S	-21.13	-54.42	**33.29**	2.10	1	4.8
$(2s2p)^3$P	-20.69		**33.73**	0.23	9	43.5
$(2p^2)^3$P	-19.33		**-**	-	9	-
$(2p^2)^1$D	-19.12		**35.30**	1.10	5	9.1
$(2s2p)^1$P	-18.88		**35.54**	0.64	3	15.6
$(2p^2)^1$S	-16.86		**37.56**	$\ll 0.1$	1	$\gg 100$

Table 1: Properties of doubly excited $He^{**}(2l2l')$ states relevant to autoionization processes. The table presents the binding energy of the initial doubly excited state (E_{b1}), and of the final $He^{+}(1s)$ state (E_{b2}) [8], along with the resulting kinetic energy of the emitted autoionization electron (E_e) calculated using Equation (3). The autoionization rates (Γ_{AI}) [9], statistical weights (g_i) and lifetimes for each initial state are also provided to approximate the relative intensities of the expected peaks, and illustrate the importance of interaction time.

These theoretical predictions are supported by previous experimental observations. Electron beam excitation studies of He gas revealed two autoionization peaks at approximately 33.5 eV and 35.6 eV [10]. Ion-surface interaction experiments conducted using Sirϕ setup in 2004 yielded energies of approximately 34.5 eV and 36.0 eV [3], showing the two-peak structure across different measurements. It should be noted that given the small energy separation between these peaks, resolving them as distinct features may prove challenging.

5.2 Spectra

The following section presents the initial electron energy spectra obtained during the recommissioning phase of the ESA. For each ion species, measurements were conducted under optimized conditions following position and parameter tuning.

The spectral analysis employs fits of a skewed Gaussian distribution (see Equation (6) in the Appendix). This distribution is particularly well-suited for secondary electron spectra, as these electrons undergo scattering and various interactions near or within the surface, resulting in characteristic asymmetric distributions with extended low-energy tails.

The Full Width at Half Maximum (FWHM) is determined numerically by finding the points where the fitted curve crosses half of its maximum height (calculated with the baseline offset taken into account), with the FWHM being the distance between these two crossing points. This approach works universally for any peak shape, making it suitable for analyzing the skewed Gaussians used here. A limitation of this method is that it does not produce results if the fit range does not fully encompass both sides of the peak where it crosses the half-maximum height (as will be the case in Figure 19a). It should also be noted that, while background subtraction would have been necessary to determine the accurate height of the peak for calculating the FWHM, making it accurate and representative, the current approach was sufficient for this study as it was only used to compare relative changes between different experimental settings and conditions.

$\mathbf{Ar}^{9+}$

For the Ar^{9+} measurements, 63 keV ions were generated using the ECRIS source and transported to Sirϕ. Initial measurements were performed without beam deceleration at $\psi = 15^\circ$ to test the ESA's operation. Figure A.7 in the Appendix demonstrates that while the detector was confirmed to be operating, no characteristic autoionization peaks were produced. Instead, the spectrum exhibited only a broad structure across the whole measurement range, with decreasing intensity. This result provided clear evidence for the necessity of beam deceleration to achieve the low ion velocities required for the expected autoionization features.

Next, the beam was decelerated using the Sirϕ setup to 2250 eV. The target was positioned at $\psi = 45^\circ$ to maximize the surface area impacted by the ion beam, enhancing the signal intensity. Upon initial deceleration, a characteristic peak around 210 eV became visible, confirming the successful observation of the autoionization electrons. However, determining the optimal target position required extensive fine-tuning (discussed in the following section). After optimization, the target was positioned at $(x, y) = (8.5, 12.0)$ mm, yielding the spectrum shown in Figure 14.

$\mathbf{He}^{2+}$

A 14 keV He^{2+} beam was transported to the Sirϕ setup and decelerated to 100 eV. The target was oriented at $\psi = 15^\circ$ relative to the incident beam to further minimize the surface-normal velocity

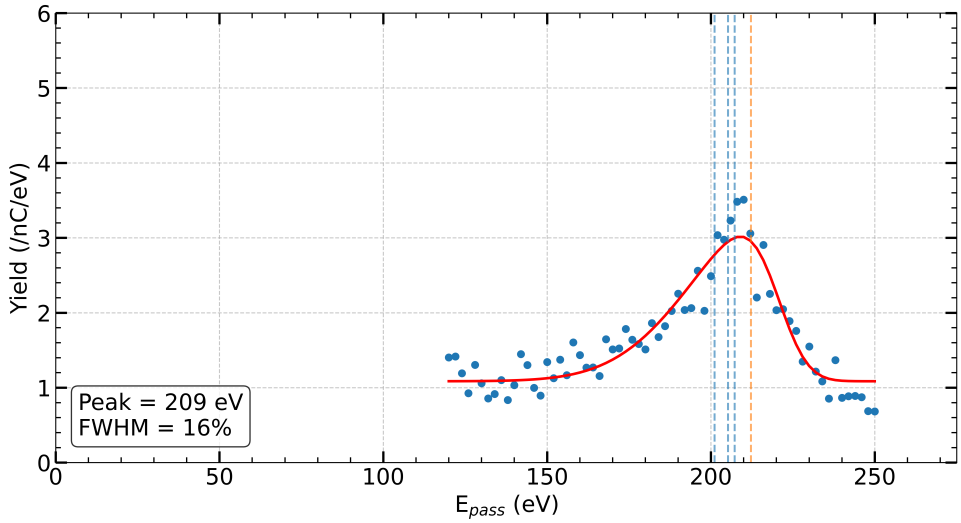

Figure 14: Electron energy spectrum for 2250 eV Ar^{9+} ions at target position $(x,y) = (8.5, 12.0)$ mm and $\psi = 45°$. The prominent peak at approximately 210 eV corresponds to autoionization electrons. The peak's energy is consistent with previous studies, indicated by the blue [7] and orange [2] dashed lines.

component. Through optimization of the target's position, the highest spectral quality was achieved at coordinates $(x,y) = (11.0, 10.0)$ mm. The resulting spectrum, presented in Figure 15, clearly reveals the expected autoionization feature predicted by theoretical calculations.

Additional test measurements on both ions species explored sample biasing effects on spectral quality: while it increased the count rate, it did not improve the peak compared to background. However, grounding the heating filament used for sample cleaning provided significant improvement and was used for all subsequent measurements.

Observed peaks from both ion species' electron spectra show excellent agreement with previous experiments and theoretical expectations. This consistency serves as an initial validation of both the ESA and the whole experimental setup employed in this study.

5.3 Target position maps

A critical observation during the initial measurements was the strong sensitivity of spectral quality to the target position. The possible reasons for this dependence will be explored in Section 6. To systematically characterize this spatial dependence, position maps were generated to quantify the peak quality at each (x,y) location across the target surface.

Several metrics were evaluated to represent peak quality, including integrated peak area, peak-to-background ratio, and peak height above baseline. After comparing these approaches with subjective visual assessment of the spectra, the height of the fitted (Equation (6)) peak's maximum above baseline was selected as the most reliable metric, showing the best correspondence with qualitative peak evaluation.

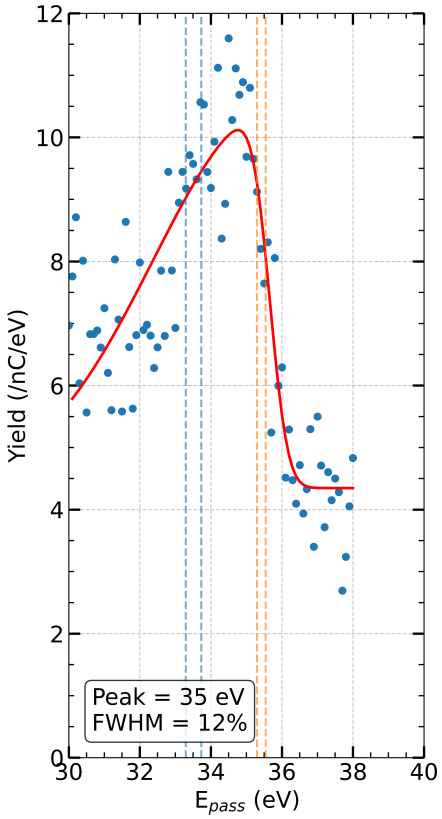

Figure 15: Electron energy spectrum for 100 eV He^{2+} ions at optimized target position $(x,y) = (11.0, 10.0)$ mm and $\psi = 15°$. The spectrum shows a wider peak around 34.8 eV, corresponding to autoionization from different doubly excited helium states. While only a single peak is visible, its energy is in good agreement with theoretical predictions indicated by blue (peak 1) and orange (peak 2) dashed lines.

He^{2+} position sensitivity

While no systematic position map was generated for He^{2+}, significant position sensitivity was also observed for this ion species. Notably, adjustments to the voltage of the final deceleration lens (lens E) dramatically altered the optimal target position, requiring repositioning after each adjustment.

Ar^{9+} position map

The prominent ~ 210 eV autoionization peak from Ar^{9+} provided an ideal feature for quantitative position optimization. Spectra were recorded across the energy range of 120-250 eV using 2 eV steps and 10 s measurement time per step. An example spectrum and its corresponding skewed Gaussian fit are shown in Figure A.8 in the Appendix, illustrating the fitting procedure used to extract peak heights for each position.

The resulting position map, shown in Figure 16, reveals the region of optimal performance for a 2250 eV Ar^{9+} beam, with the sample at $\psi = 45°$ and the ESA at $\theta = 90°$. The map orientation corresponds to the experimental geometry depicted in Figure 6, with linear interpolation applied between measurement points to enhance visualization. A broad region of high peak quality is observed within the coordinates $9.0 \leq x < 11.0$ mm and $10.5 \leq y \leq 11.5$ mm, with a gradual degradation in quality outside this zone.

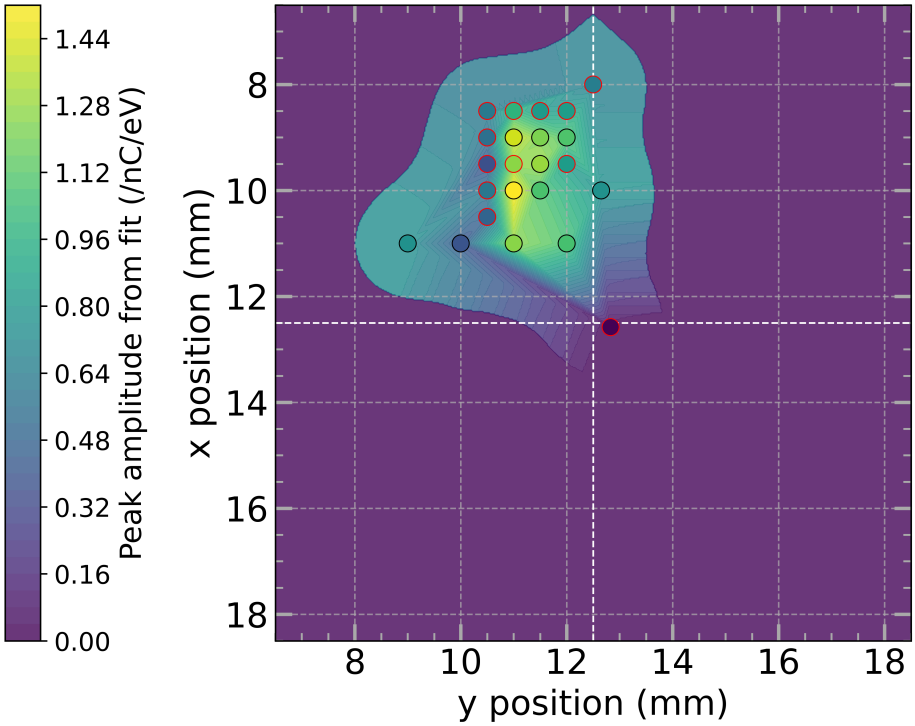

Figure 16: Position map showing the quality of the autoionization peak across different target positions for Ar^{9+} secondary electrons. The color scale represents the fitted peak height above baseline, with each dot being a measurement location. The optimal region extends from $x = 9.0 - 11.0$ mm and $y = 10.5 - 11.5$ mm, providing a relatively broad area for stable measurements. The center of the manipulator's range is indicated to aid comparison between different position maps. An example of the fitting procedure used to extract peak heights is shown in Figure A.8 in the Appendix.

This position mapping approach proved effective for identifying optimal measurement locations, though it was time-intensive. A critical limitation was found when beam energy or deceleration lens settings were altered: the previously optimal position would no longer yield the best spectral quality, necessitating complete remapping. This behavior indicates that the ion beam profile and focal properties are highly sensitive to these experimental parameters, highlighting the need for improved stability in future measurements.

6 Calibration of the ESA

Following the successful initial measurements described in the previous section, a comprehensive series of improvements were implemented to enhance the performance and consistency of the Sirϕ setup. This section details these modifications and presents the subsequent measurements that demonstrate their effectiveness.

6.1 Setup improvements

The optimization process addressed several key aspects of the experimental configuration, each targeting specific performance limitations identified during the initial measurements.

Beam collimation and alignment

A critical improvement involved the installation of a second collimating diaphragm just before the beam enters the experimental chamber, positioned after the deceleration lens system and the first diaphragm, as illustrated in Figures 5a and 17. This addition was motivated by the previously observed substantial beam divergence at large deceleration factors [3]. The additional collimator serves a dual purpose: reducing beam divergence to maintain a well-defined beam profile and eliminating potential asymmetric effects from the deceleration lenses that could introduce unwanted beam deflection.

Next, the entire setup underwent careful realignment with respect to the beamline axis to ensure optimal beam transmission through all elements. This procedure significantly increased the ion current reaching the target and thus improving yield count statistics . At the same time, the ESA was precisely aligned to the chamber center and beamline height, guaranteeing that its field of view remains consistently directed at the same target location as it moves along its track. The schematic comparison shown in Figure 17 demonstrates the enhanced beam focusing achieved through all of these modifications.

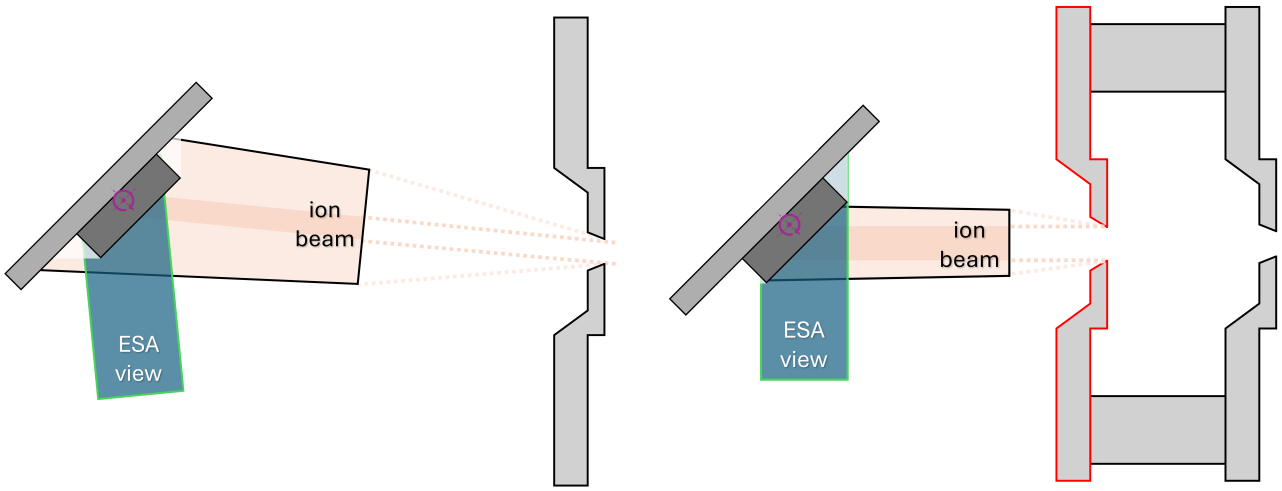

(a) (b)

Figure 17: Comparison of the Sirϕ setup showing the implemented improvements. Original setup (a) shows the effects of beam divergence and misalignment. (Note that the inaccuracies are exaggerated.) Improved configuration (b), highlighting the addition of the second collimating diaphragm (red outline), the realigned ion beam and ESA field of view.

Magnetic interference elimination

During the alignment process, it was discovered that an ionization pressure gauge containing a strong permanent magnet was positioned above the deceleration zone. The magnetic field from this gauge could deflect the ion beam trajectory, particularly affecting the low-energy ions after deceleration. To eliminate this interference, the gauge was relocated to the far side of the setup, away from the ion beam's direct path.

Improving the vacuum

As these modifications required exposing the system to atmospheric conditions, a comprehensive bakeout procedure was necessary. The entire setup was heated to temperatures exceeding 100°C for more than 24 hours, successfully reducing the chamber's pressure from 10^{-8} mbar to the 10^{-10} mbar regime compared to conditions before opening it up. The improved vacuum conditions minimize residual gas coating of the target surface and reduce scattering collisions with low-energy electrons, both critical for obtaining clean autoionization spectra with minimal background effects.

6.2 Spectra

All subsequent measurements mentioned were performed with consistent geometric parameters: the target maintained at $\psi = 45^\circ$ and the ESA positioned at $\theta = 90^\circ$ to ensure comparability.

Ar^{9+}

The 63 keV Ar^{9+} ion beam was initially decelerated to 2250 eV, and the first measurement shown in Figure 18a was acquired at position $(x,y) = (12.5, 12.5)$ mm. Remarkably, this measurement immediately revealed a well-defined autoionization peak without requiring extensive positional optimization. The high ion intensity has also enabled significantly shorter measurement times per energy step while maintaining adequate counting statistics.

Next, the ion beam was further decelerated to 450 eV, a deceleration factor at which previously it was not possible to acquire the autoionization electrons with the ESA. This lower impact energy resulted in a substantial increase in autoionization electron yield due to enhanced interaction times at reduced velocities.

At the optimized position of $(x,y) = (11.1, 13.3)$ mm, five consecutive one-hour measurements were performed and subsequently averaged to minimize statistical fluctuations, yielding the high-quality spectrum presented in Figure 18b. The resulting peak, centered at approximately 207 eV, demonstrates excellent agreement with established literature values [7], and shows only minimal deviation from previous surface interaction experimental values [2].

While the background levels were substantially reduced, the FWHM of the autoionization peak remained essentially unchanged, measuring 17.8% compared to the previous value of 17.6% before the adjustments to the setup.

He^{2+}

The 14 keV He^{2+} ion beam was decelerated to 100 eV, and initial measurements were conducted at position $(x,y) = (10.5, 13.5)$ mm following some positional tuning, as shown in Figure 19a. However, the improvements in beam current and counting rates were less pronounced for this ion species

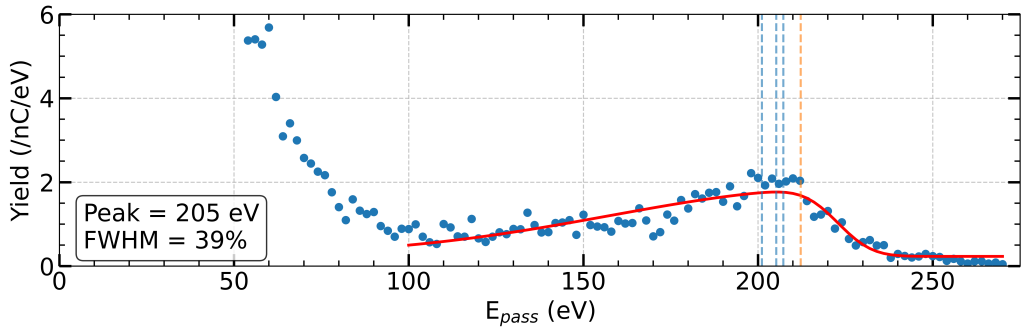

(a) Ar^{9+} at 2250 eV

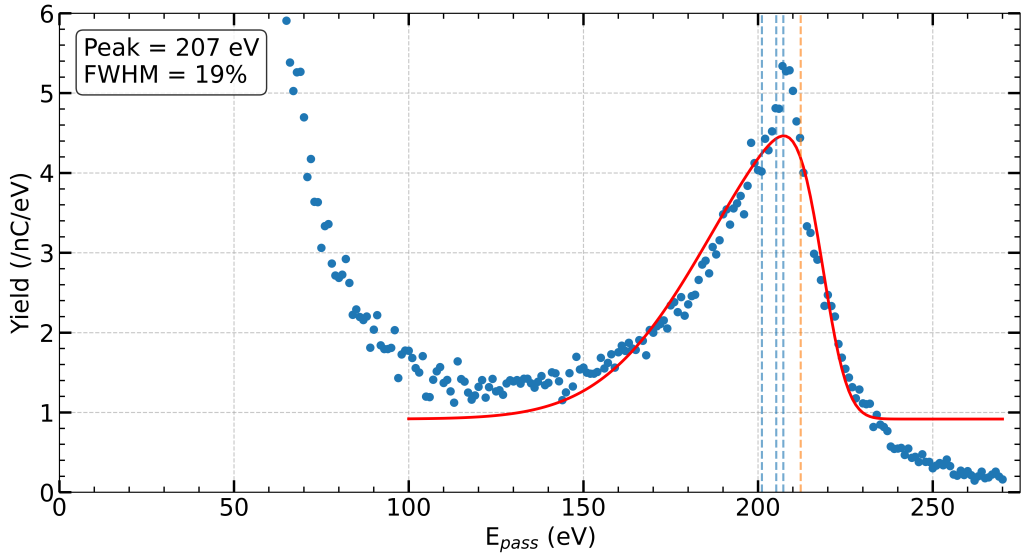

(b) Ar^{9+} at 450 eV

Figure 18: Secondary electron spectra from Ar^{9+} ions at 2250 eV (a) and 450 eV (b) beam energies. The electron spectra demonstrate improved signal quality after setup optimization, while the lower energy one shows significant improvements, with the main autoionization peak centered around 207 eV. The peak's energy is consistent with previous studies, indicated by the blue [7] and orange [2] dashed lines. Note that (b) was taken over 5 hours to reduce fluctuations in the measured yield.

compared to Ar^{9+}, with some measurements showing reduced performance relative to the original configuration.

Further deceleration to 10 eV was successfully achieved, representing a significant accomplishment given the challenges associated with maintaining beam coherence at such low energies. This ultra-low impact energy produced a significant increase in autoionization electrons, confirming theoretical expectations for enhanced interaction times at low energies. The optimal measurement position was confirmed to be $(x, y) = (10.5, 13.5)$ mm, and yielded the spectrum presented in Figure 19b.

The dominant autoionization peak, centered at 35.5 eV, shows excellent agreement with both theoretical calculations and experimental literature values [3, 10]. However, the expected double peak structure could not be fully resolved, as the two autoionizing states are separated only by a small energy interval.

Compared to the previous measurements at 100 eV (Figure 15), the background was dramatically reduced and the measurement stability significantly improved, although the FWHM increased slightly.

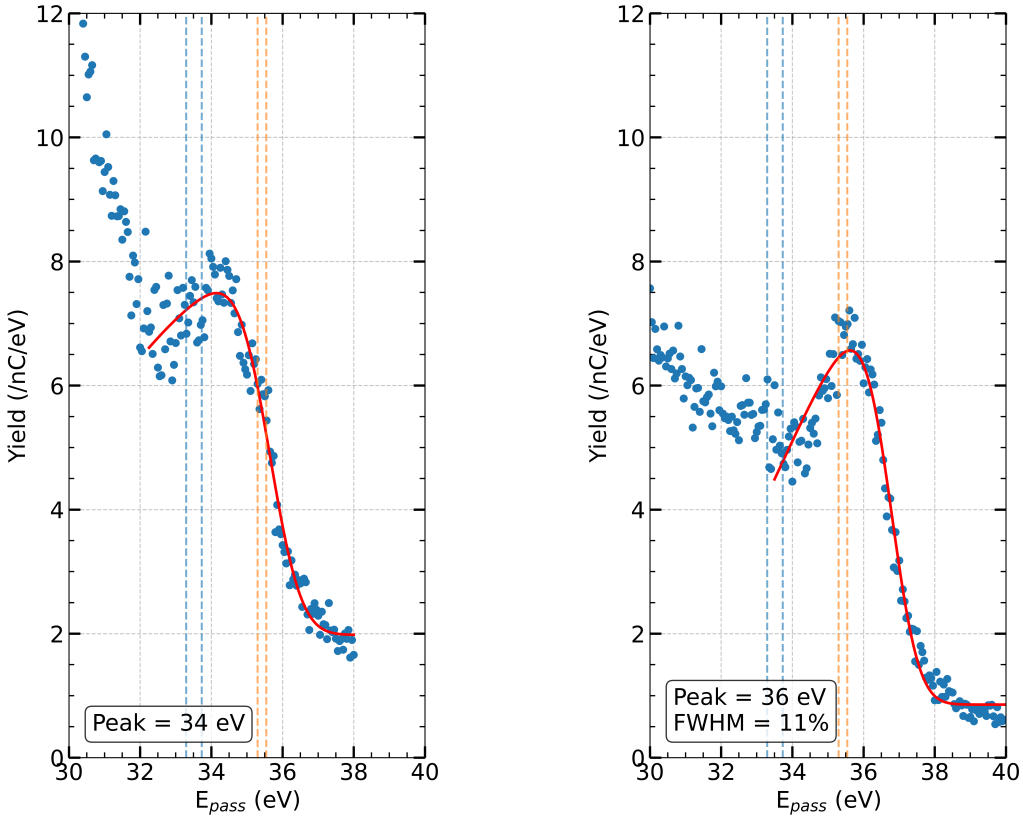

(a) He^{2+} at 100 eV

(b) He^{2+} at 10 eV

Figure 19: Electron spectra from He^{2+} ions at 100 eV (a) and 10 eV (b) impact energies. The spectrum in (b) demonstrates successful deceleration, with the main autoionization peak centered at 35.5 eV. The closely spaced double peak structure remains unresolved.

When looking at the spectra from both ion species it is clear that the implemented modifications successfully enhanced both the quality and intensity of autoionization features. This improvement was primarily achieved through the ability to decelerate ions to lower energies, and with that increasing the interaction times. This low-energy operation was made possible by the consistent optimal measurement positions across different energies.

However, it should be noted that both ion species exhibit regions of high intensity that dominate the lower energy regimes: below 120 eV for 450 eV Ar^{9+} (Figure 18b) and below 15 eV for 10 eV He^{2+} (Figure 20). While a detailed investigation of this phenomenon is beyond the scope of this study, the most likely explanation is contributions from kinetic and Auger electrons. The energy resolution correction; dividing the yield by $\Delta E = E_{\text{pass}} \times 0.5\%$, may further enhance this effect and warrants future investigation to establish the ultimate limits of low-energy measurements.

6.3 Target position maps

To assess the improvements achieved through setup modifications, positional maps were recorded for both ion species. These maps clearly demonstrate enhanced beam focusing and improved measurement consistency across the range of studied ions and energies.

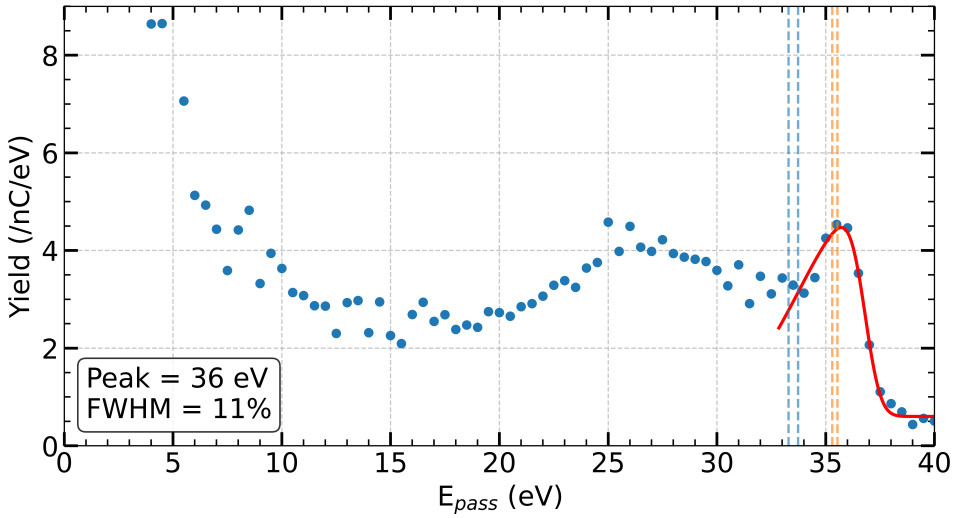

Figure 20: Complete electron spectrum from He^{2+} ions at 10 eV impact energy covering the full range from 0-40 eV. This measurement was performed with a relatively large energy step of 0.5 eV. The spectrum clearly shows the autoionization peak centered around 36 eV, while also demonstrating the characteristic high-intensity behavior at low energies (below 15 eV) that is consistent with observations in both Ar^{9+} measurements (Figure 18).

Ar^{9+}

Complete electron energy spectra spanning 0 to 270 eV were acquired using the 450 eV Ar^{9+} ion beam across a range of target positions. The measurements used 3 eV energy steps with 2 s acquisition time per step to balance spectral resolution with reasonable measurement duration. The quality metric was determined by fitting a skewed Gaussian function to the autoionization peak region (95-270 eV) and extracting the peak height as the figure of merit, same as in Section 5.3.

The positional survey was conducted systematically, beginning from the initial position $(12.5, 12.5)$ mm and adjusting x and y in steps of 0.5 to 1 mm. The search pattern alternated between sweeping along the two axes until the optimal position was identified, with additional strategic points measured to map the peak quality distribution. The resulting positional map is presented in Figure 21a.

While the maximum peak height was initially recorded at position $(x, y) = (11.1, 13.3)$ mm, longer measurements with smaller steps (Figure 18b) later revealed this to be an outlier. When incorporating this new data, the consistently optimal region is around $(x, y) \approx (10.3, 13.0)$ mm.

Comparison with the original positional map (Figure 16) reveals two significant improvements: substantially increased peak heights and a more tightly focused region of optimal performance. These findings confirm the effectiveness of the setup modifications in enhancing the experimental results.

He^{2+}

Position maps were generated for He^{2+} ions at both 100 eV and 10 eV impact energies. Given the narrower linewidths characteristic of helium autoionization features, energy step sizes smaller than 1 eV were employed with various acquisition times (2-10 s per step) to ensure adequate spectral resolution and counting statistics.

Remarkably, the optimal position for both beam energies was consistently determined to be $(x, y) = (10.5, 13.5)$ mm. This reproducibility across different energies highlights a key advantage of the improved setup: the elimination of energy-dependent beam effects that previously required position op-

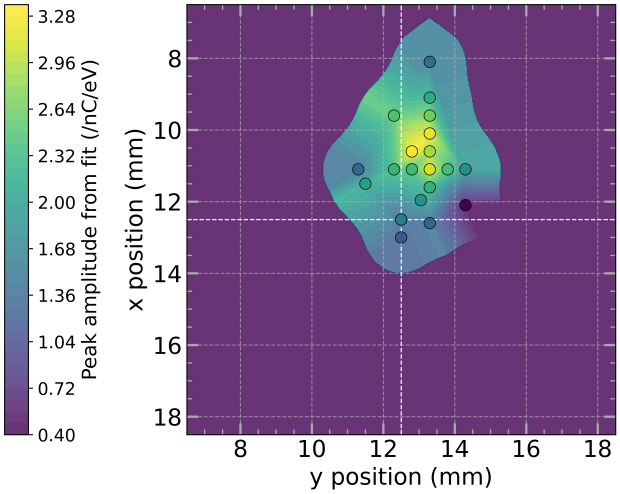

(a) Ar^{9+} at 450 eV

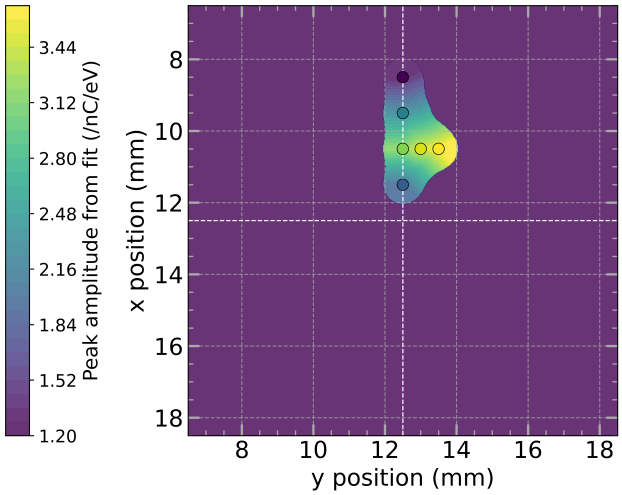

(b) He^{2+} at 100 eV

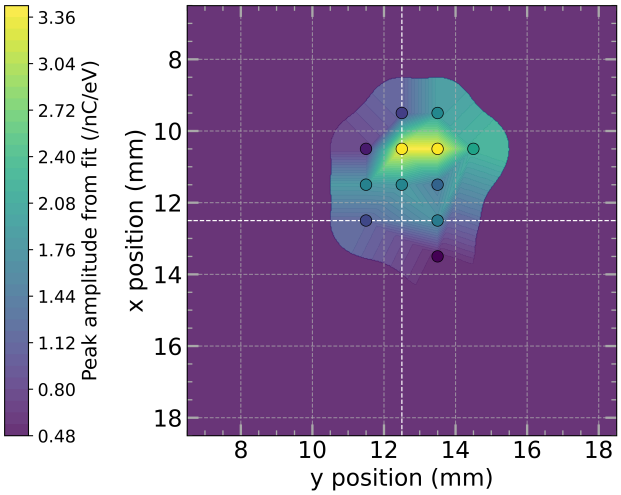

(c) He^{2+} at 10 eV

Figure 21: Position-dependent autoionization peak intensity maps for Ar^{9+} ions at 450 eV (a), He^{2+} ions at 100 eV (b), and He^{2+} ions at 10 eV (c) impact energies. The color scale represents fitted peak heights, as detailed in Section 5.3 and Figure A.8 in the Appendix. All maps show well-focused regions of high values with remarkable consistency in optimal measurement positions across different ion species and energies, demonstrating the effectiveness of the setup improvements.

timization for each experimental condition. The positional maps for 100 eV and 10 eV measurements are shown in Figures 21b and 21c, respectively.

The comparison between these maps further emphasizes the focused high-quality measurement region and its consistency across energy scales. This energy independence represents a significant advancement, as it eliminates the need for time-consuming position optimization when changing experimental parameters.

An overview of the positional analyses presented in Figure 21 demonstrates that the high-quality spectroscopy regions are now remarkably similar across different ion species and energies. This consistency confirms that the implemented improvements have successfully addressed the issues that

previously limited experimental capabilities. Importantly, the same spectroscopic quality is now expected for secondary electron energies at least as low as the 30 eV regime, regardless of the ion energy used to produce them. This demonstrated consistency in optimal positions across species and energies eliminates the need for extensive position tuning when transitioning between different experimental settings, enabling investigations of various ion-surface combinations with predictable performance at the established target position regions.

7 Conclusion

This thesis presents a comprehensive study of the recommissioning and calibration of an electrostatic analyzer (ESA) for secondary electron spectroscopy in ion-surface interactions. The work successfully demonstrated the low energy electron measurement capabilities of the Sirϕ experimental setup at ZERNIKELEIF, enabling precise characterization of electron emission from ion-surface collisions.

The SIMION simulations provided crucial insights into the ESA's operational characteristics. The systematic parameter optimization revealed that the proportionality factor F and voltage ratio V_{ratio} exhibit linear relationships with energy accuracy, with optimal values of $F = 6.40$ and $V_{ratio} = -0.910$ determined for this simulated detector. An important finding was an energy-dependent deviation in pass energy, showing a systematic shift from the calibrated +0.04% at 35 eV to -3.53% at 35 keV. This energy dependence has important implications for spectroscopic measurements taken further away from the calibration energy. Additionally, the simulations demonstrated that electron starting positions influence the transmitted energy distribution, with particles originating from near the top of the acceptance window contributing to asymmetric spectral broadening.

The experimental measurements successfully demonstrated the detection of characteristic autoionization electrons from both Ar^{9+} and He^{2+} ions. For Ar^{9+}, the prominent autoionization peak centered at approximately 207 eV showed excellent agreement with previous experimental studies. The He^{2+} measurements revealed a single autoionization feature centered around 34-36 eV, with energies matching the range of the two expected peaks, though the closely spaced double peak structure could not be resolved. These results validate both the ESA and the experimental approach employed in this study.

The comprehensive setup improvements implemented during the calibration phase significantly enhanced measurement quality and consistency. The installation of a second collimating diaphragm, careful realignment of the entire system, elimination of magnetic interference, and improved vacuum conditions collectively enabled successful ion deceleration to much lower energies. These low ion velocities resulted in dramatically increased autoionization electron yields due to longer interaction times, as demonstrated by the measurements of 10 eV He^{2+} and 450 eV Ar^{9+} ions compared to previous higher energy measurements.

A critical finding was the inconsistent but strong position dependence of spectral quality observed during initial measurements, which was successfully addressed through the setup improvements. The new position mapping studies revealed that optimal measurement locations became remarkably consistent across different ion species and energies after the modifications. This consistency eliminates the need for extensive position optimization when changing experimental parameters, significantly improving the experimental workflow.

This study established a solid foundation for future secondary electron spectroscopy studies, demonstrating the capability to measure autoionization electrons with energies as low as 30-35 eV and achieving consistent optimal positioning across different ion species and energies. The systematic approach developed here, combined with the improved experimental stability, positions Sirϕ to tackle the challenging measurement of Sn ion induced secondary electrons, which remain crucial for advancing EUV lithography technology.

Outlook

This study has established a solid foundation for future secondary electron spectroscopy investigations, with several opportunities for further enhancement and application.

The energy-dependent deviation observed in simulations suggests that implementing energy-dependent corrections to the F and V_{ratio} parameters could improve measurement accuracy across the full operational range. Additionally, the recorded spectra's quality could be further enhanced through data processing techniques, such as noise reduction algorithms, and background subtraction methods [6].

Future investigations could explore the high-intensity regions observed at low energies in both ion species, which likely originate from kinetic and Auger electrons. Understanding these contributions would help establish the ultimate limits of low-energy measurements and optimize experimental conditions for this region. Additionally, the setup's enhanced capabilities open possibilities for studying other ion-surface combinations relevant to plasma physics and surface science applications.

The successful recommissioning of the ESA for electron measurements represents the restoration of valuable experimental capabilities at ZERNIKELEIF, providing an effective tool for investigating secondary electrons from ion-surface interaction processes across a wide range of energies and species.

Acknowledgments

I would like to express my sincere gratitude to Ronnie Hoekstra for providing me with the opportunity to conduct my bachelor research project in the QISD group and being my supervisor. I am also grateful to Thomas Schlathölter for serving as the second examiner and dedicating time to review this thesis.

I am infinitely thankful to Luc for his exceptional supervision and guidance throughout this project. His dedication to ensuring every aspect of my research experience went smoothly and his genuine investment is amazing. It was really nice working together.

I would also like to thank Pedro for his help in familiarizing me with both the experimental setup and the research group, as well as for being excellent company during lunch breaks. Many thanks to Mart for his explanations of various technical challenges I encountered, and for sharing insights into others that were equally fascinating, and also for the biology fun-facts.

Finally, I want to thank the entire QISD group for their welcoming attitude and inclusive environment. The lunch walks and numerous coffee breaks provided perfect opportunities to break from routine and made this research experience both social and enjoyable. This experience has really made me think about eventually returning to the field of physics.

References

[1] V. Y. Banine, K. N. Koshelev, and G. H. P. M. Swinkels, "Physical processes in EUV sources for microlithography", *Journal of Physics D: Applied Physics* **44**, 253001 (2011).

[2] S. de Zwart, A. Drentje, A. Boers, and R. Morgenstern, "Electron emission induced by multiply charged Ar ions impinging on a tungsten surface", *Surface Science* **217**, 298 (1989).

[3] D. F. A. Winters, "Polarization transfer in ion-surface scattering", PhD thesis (2004).

[4] A. Arnau, F. Aumayr, P. M. Echenique, M. Grether, W. Heiland, J. Limburg, R. Morgenstern, P. Roncin, S. Schippers, R. Schuch, N. Stolterfoht, P. Varga, T. J. M. Zouros, and H. Winter, "Interaction of slow multicharged ions with solid surfaces", *Surface Science Reports* **27**, 113 (1997).

[5] P. Apell, "Surface plasmon de-excitation of multiply charged ions", *Journal of Physics B Atomic Molecular and Optical Physics* **21**, 2665 (1988).

[6] L. Folkerts, "Charge exchange of multiply charged ions with metal surfaces", PhD thesis (1992).

[7] L. O. Werme, T. Bergmark, and K. Siegbahn, "The $L_{2,3}MM$ auger spectrum of argon", *Physica Scripta* **8**, 149 (1973).

[8] S. Bashkin and J. O. Stoner, *Atomic energy levels and grotrian diagrams*, Vol. 1 (North Holland, 1975).

[9] P. Hicks and J. Comer, "Ejected electron spectroscopy of autoionizing states excited by low energy electron impact", *Journal of physics* **8**, 1866 (1975).

[10] N. Oda, S. Tahira, F. Nishimura, and F. Koike, "Energy and angular distribution of electrons ejected from autoionization states in helium by electron impact", *Physical Review A* **15**, 574 (1977).

Appendix

Simulations of the ESA

Determining the energy distribution for fitting $E_{observed}$

Particles were recorded when passing through the plane (x=62.25 mm, thin red line in Figure A.1), this is between the MCP front and the grounding diaphragm before it. All particles also pass this plane just before second entry diaphragm. From these two factors, the initial energy could be determined (as the MCP front voltage accelerates the particles before their impact), and matched to each particle's second pass. So the observed energy distribution includes all particles that passed through twice this x-plane, and their energies are assigned based on the energy they had when first being recorded. Finally, a Gaussian is fitted to this distribution.

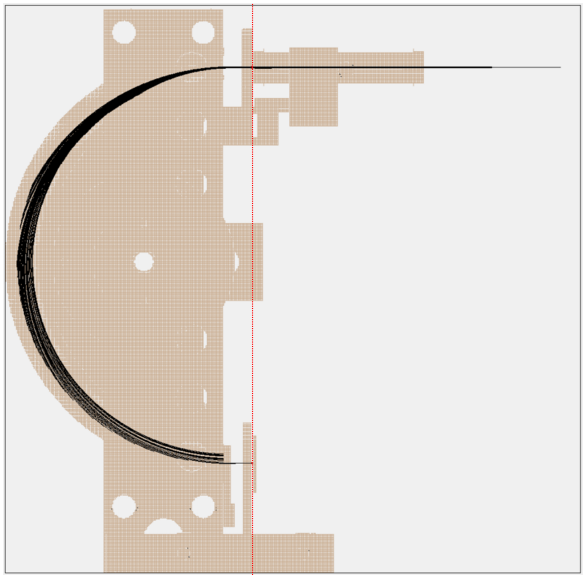

Figure A.1: The vertical red line indicates the line of recording, while the semi-circular black lines are the paths of the individual simulated particles, starting from a single point here.

Additional plots

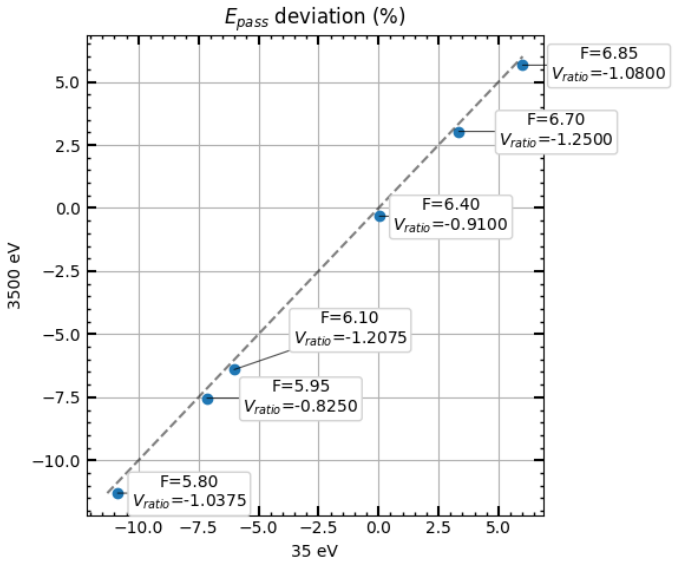

Figure A.2: Correlation of E_{pass} deviation between 35 eV and 3500 eV simulations for identical F and V_{ratio} parameter combinations. The strong linear correlation (indicated by the diagonal trend) confirms that the optimization parameters are energy-independent, validating the electrostatic principles underlying the ESA operation. Note that there is a small downward shift of all points, indicating a slightly lower $E_{observed}$ for 3500 eV, for more details on this see Section 4.2.

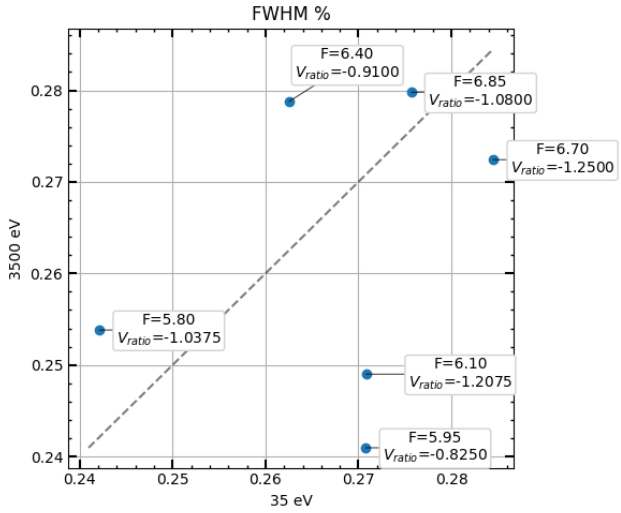

Figure A.3: Correlation of FWHM values between 35 eV and 3500 eV simulations. The absence of correlation reflects the lack of systematic dependence of energy resolution on the optimization parameters F and V_{ratio}, consistent with the observations at lower energy regimes, shown in Figure A.4.

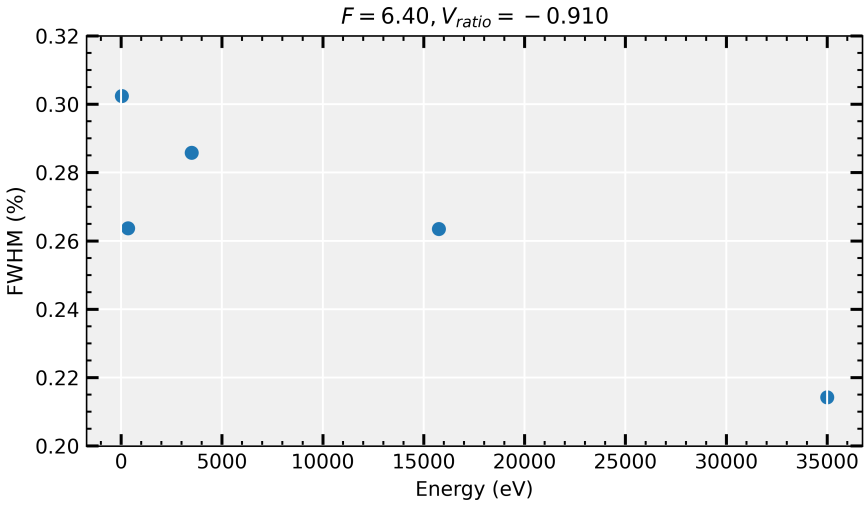

Figure A.4: Energy resolution (FWHM) as a function of different energy regimes showing a slight downward trend. While the resolution appears to improve marginally at higher energies, the variation remains within the range observed during parameter optimization (see e.g. Figure 8b), preventing definitive conclusions about energy-dependent resolution changes.

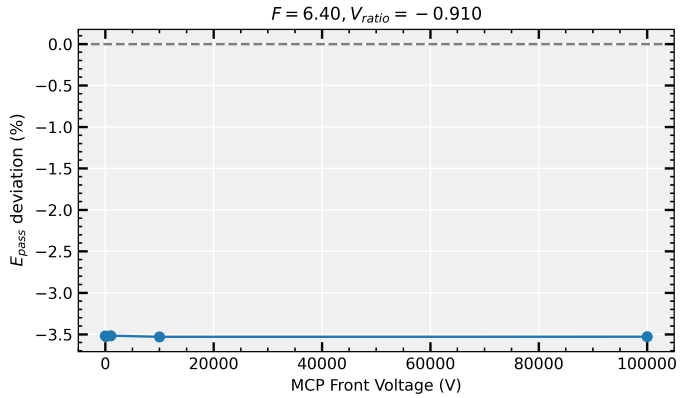

(a)

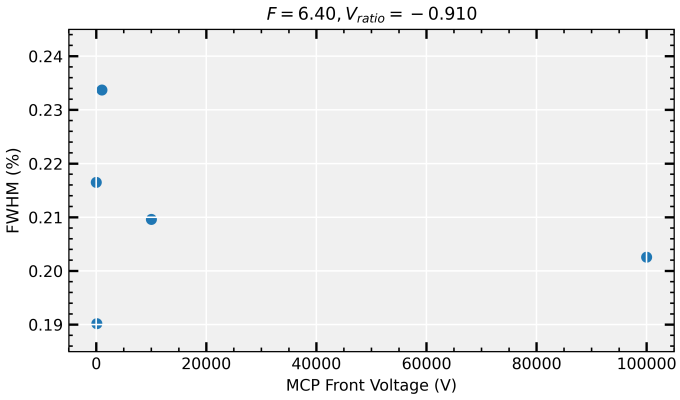

(b)

Figure A.5: Investigation of MCP front voltage influence on ESA performance at $E_{pass} = 35$ keV. Both energy deviation (a) and FWHM (b) show no systematic dependence on the MCP front voltage, confirming that the observed energy-dependent behavior is independent from this parameter. The same was observed for E_{pass}=35 eV as well.

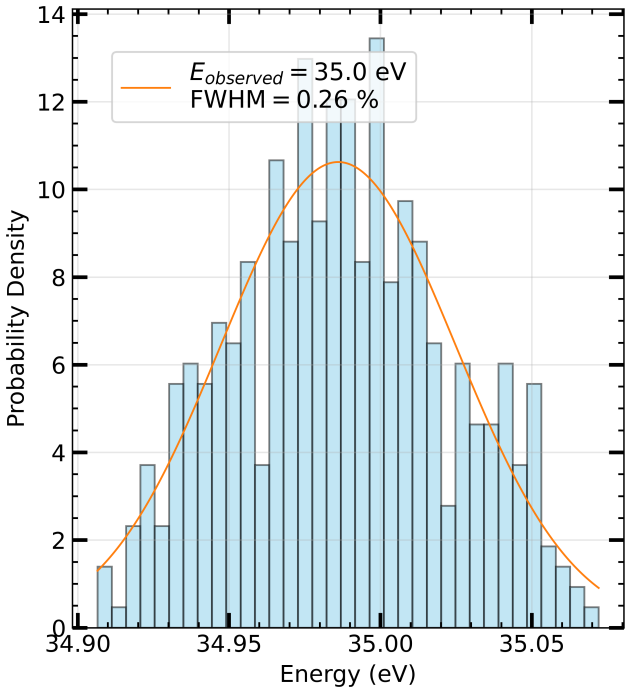

Figure A.6: Energy distribution of electrons transmitted through the ESA when all particles are initialized from a single point source. Unlike the sphere starting distribution case of Figure 11, this spectrum shows a symmetric Gaussian profile, demonstrating that the asymmetric broadening observed there is related to the wider range of starting locations.

Recommissioning the ESA for electrons

Skewed Gaussian fit for peak height

For fitting to the peaks a skewed Gaussian was fitted:

$$f(E) = \frac{A}{2} \exp\left(-\frac{(E-\mu)^2}{2\sigma^2}\right) \cdot \left[1 + \operatorname{erf}\left(\frac{\alpha(E-\mu)}{\sigma\sqrt{2}}\right)\right] + C, \tag{6}$$

where A represents the amplitude, μ the center position, σ the standard deviation, α the skewness parameter ($\alpha < 0$ creates tails toward lower energies), and C the baseline offset. The peak height used to color the position maps was determined by numerically finding the highest point of the fit and subtracting the baseline offset (C) from it.

Additional plots

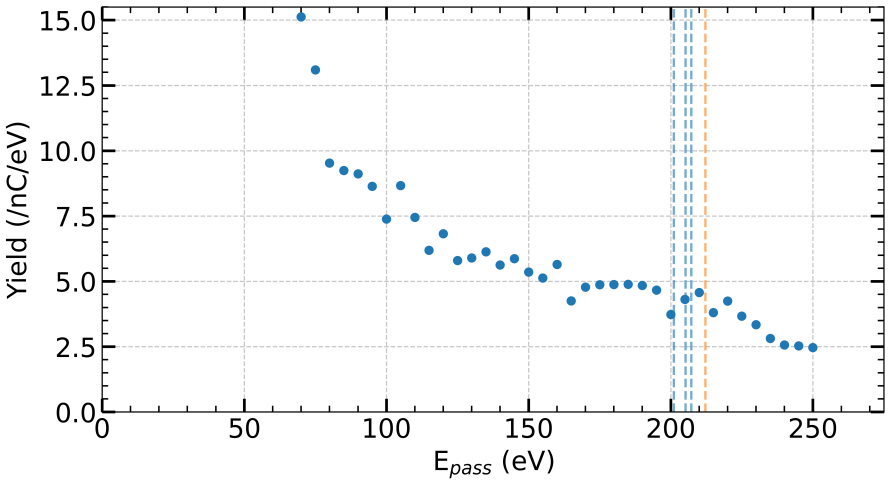

Figure A.7: Electron energy spectrum for 63 keV Ar^{9+} ions impacting the surface without deceleration at $\psi = 15°$. The spectrum shows only broad features with no distinct autoionization peaks, demonstrating the necessity of beam deceleration.

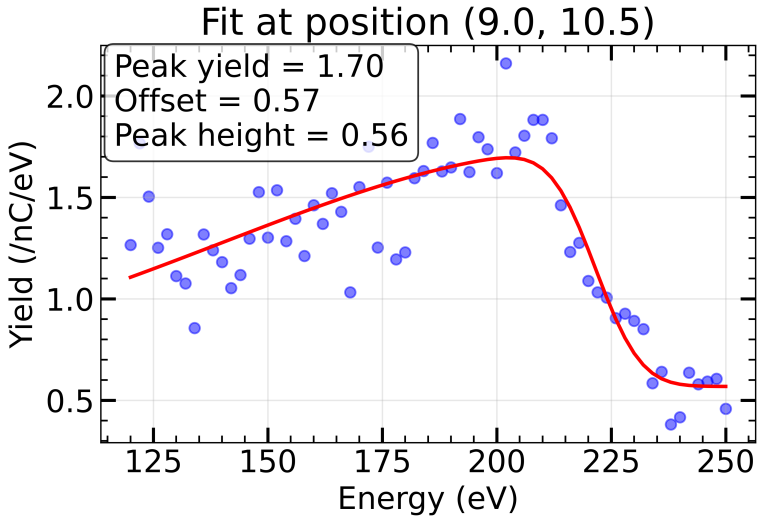

Figure A.8: Example electron energy spectrum of the characteristic autoionization peak with the fitted skewed Gaussian function. The peak height above baseline, determined numerically from such fits, served as the quality metric for position mapping described in Section 5.3.